DEGREE PROJECT IN ENGINEERING PHYSICS,
SECOND CYCLE, 30 CREDITS
STOCKHOLM, SWEDEN 2019

Investigation of IR transmittance in different weather conditions and simulation of passive IR imaging for flight scenarios

JOSEFINE CORNÉ

ULRIKA HELANDER SJÖBLOM

KTH ROYAL INSTITUTE OF TECHNOLOGY
SCHOOL OF ENGINEERING SCIENCES

Investigation of IR transmittance in different weather conditions and simulation of passive IR imaging for flight scenarios

JOSEFINE CORNÉ
ULRIKA HELANDER SJÖLBLOM

Master thesis at Saab, Avionics Systems
Supervisor at Saab: Erasmus Cedernaes
Supervisor at KTH: Lars-Gunnar Andersson
Examiner: Fredrik Laurell

TRITA-SCI-GRU 2019:109

Abstract

In aviation, safety is critical. Aircraft operations, such as approach and landing, in adverse weather conditions can be a difficult task. In addition, authorities strictly regulate operations when the visibility is below certain threshold values. In order to improve the situational awareness of pilots, IR technology might be beneficial since IR radiation in many cases penetrate darkness and different weather conditions better than visible light. The objective of the thesis project was to investigate if IR technology could improve landing possibilities in adverse weather conditions. This thesis project was divided in two parts. The first covering an investigation of the transmittance of IR radiation through different states of the atmosphere, i.e. different aerosol models, radiative/advective fog and rain. The second part was to create a simplified imaging IR simulator. As an introduction, the basic theory of IR radiation and extinction, in the form of absorption and scattering, together with flight systems and sensors are covered.

In the first part, the transmittance was simulated using the radiative transfer code MODTRAN. The transmittance spectra were analyzed and discussed based on the extinction theory. For radiative fog, the transmittance was observed to be higher in the LWIR interval, 8-14 µm, compared to shorter wavelengths such as visible, SWIR and MWIR. From this investigation, LWIR cameras could be beneficial in radiative fog, while in advective fog, the particles exhibit a larger size distribution and therefore scatter strongly even in the IR range. For different rain intensities, the scattering appears to be equal throughout the spectrum, and thus IR cameras exhibit no obvious advantages. The IR detection ranges in fog were calculated in MWIR and LWIR and compared to the runway visual range defined at 550 nm.

The second part was to create a simplified imaging IR simulator including a basic ground surface classification, a surface temperature model, atmospheric propagation of IR radiation simulated with MODTRAN, and finally limitations in the IR sensor were considered. These parts combined eventually led to the possibility to construct simulated IR images of the runway from an aircraft approaching Skavsta airport. For demonstrational purpose, a simulated image corresponding to a foggy day in January, with visibility set at 350 m was created. However, the weather parameters and the location can be altered to generate other desired approach situations.

Sammanfattning

När det handlar om luftfart är säkerhet av yttersta vikt och flygsäkerhetsarbete har högsta prioritet. Att landa ett flygplan i dåligt väder kan vara en stor utmaning, dessutom är det strängt reglerat vad som är tillåtet vid inflygningar när sikten är begränsad. Beroende på siktförhållandena måste piloten bekräfta visuell kontakt med landningsbanan eller tillhörande ljusanordning på angiven höjd för att få fortsätta inflygningen. Vid sådana tillfällen skulle IR-kameror kunna vara fördelaktiga eftersom IR-strålningens egenskaper skiljer sig från dem hos synligt ljus. Målet med detta examensarbete var att undersöka om IR-kameror kan förbättra landningsmöjligheterna i väderförhållanden med begränsad sikt. Projektet utgjordes av två delar, varav den första delen var en undersökning av hur IR-strålning transmitteras vid olika väderförhållanden, bland annat strålnings- och advektionsdimma samt olika regnintensiteter. I den andra delen av projektet gjordes en förenklad simulator med syfte att generera IR-bilder. Som introduktion presenteras teori kring IR-strålning, absorption och spridning av strålning, olika flygsystem samt sensorer.

I den första delen av projektet simulerades transmittansen av IR-strålning genom atmosfären med simuleringsverktyget MODTRAN. För strålningsdimma var transmittansen högre i långvågig IR, 8-14 µm, jämfört med kortare våglängder som kortvågig samt mellanvågig IR. Långvågiga IR-kameror skulle alltså kunna vara fördelaktiga i ett sådant scenario. Advektionsdimma uppvisar däremot en bredare partikelstorleksfördelning gentemot strålningsdimma, vilket innebär att strålningen sprids mer, både i det synliga- och IR-spektrumet. För de olika regnintensiteterna som undersöktes, var transmittansen ungefär lika stor över hela våglängdsspannet, vilket innebär att en IR-kamera inte har några uppenbara fördelar i det sammanhanget. En jämförelse för räckvidden av en IR-kamera gjordes mot sikten vid landningsbanan, vilken är definierad för en våglängd på 550 nm.

I den andra delen av projektet gjordes en förenklad simulator med syfte att generera IR-bilder. Den utgjordes av en markklassificering, en temperaturmodell för att bestämma marktemperatur, simulering av IR-propagering i atmosfären med hjälp av MODTRAN och till sist togs sensoregenskaper i beaktning innan bilden genererades. För att demonstrera IR-simulatorns funktion simulerades en inflygning till Skavsta flygplats en dimmig dag i januari med en sikt på 350 meter. Väderparameterar och flygplats kan dock ändras för att generera andra önskade inflygningsbilder.

Acknowledgements

There are a few persons who deserve a special acknowledgment for their contribution to this thesis. We would first of all like to thank our supervisor at Saab, Erasmus Cedernaes, for his engagement and valuable input. We have had rewarding discussions which has lead to great feedback and guidance. We would also like to thank the people at Avionics Systems in Järfälla for their hospitality, their involvement in the project and for always being available for questions.

We are also very grateful for the help from our supervisor at KTH, Lars-Gunnar Andersson. He has invested a lot of time and provided valuable feedback and thoughts throughout the course of the project.

Acronyms

AGT	Atmosphere Generator Toolkit
DH	Decision Height
EFVS	Enhanced Flight Vision Systems
FAA	Federal Aviation Administration
FLIR	Forward Looking Infrared
FPA	Focal Plane Array
GIS	Geographic Information System
GPS	Global Positioning System
HUD	Head-Up Display
ICAO	International Civil Aviation Organisation
IR	Infrared
LST	Land Surface Temperature
LWIR	Long-Wave Infrared
MAE	Mean Absolute Error
MLS	Microwave Landing Systems
MMWR	Millimeter-Wave Radar
MODTRAN	MODerate resolution atmospheric TRANsmission
MWIR	Mid-Wave Infrared
NETD	Noise Equivalent Temperature Difference
NOAA	National Oceanic and Atmospheric Administration
PMMW	Passive Millimeter Wave
RMSE	Root-Mean-Square Error
RTE	Radiative Transfer Equation
RVR	Runway Visibility Range
SiTF	Signal Transfer Function
SMHI	Swedish Meteorological and Hydrological Institute
SWIR	Short-Wave Infrared

Contents

1 Introduction

1.1 Background

Safety demands placed on an aircraft's technical systems are extremely high. Reduced situational awareness, particularly due to poor visibility, is one of the main reasons why accidents occur. Landing under unfavourable weather conditions can be a difficult task, even if the airfields are well known to the pilots.

Sensor technology plays an increasing role in modern aircraft and helps the pilot understand the surrounding environment. Different types of electro-optical sensors can be of great help in adverse weather conditions. Input from sensors such as visual cameras, infrared cameras and radar can increase the level of situational awareness and thereby contribute to safety. Military aviation has utilized infrared imaging for some time now, and with infrared sensors becoming more readily available, they are now a viable option for civil aviation applications.

Fog and precipitation are the principle obstacles in flying scenarios, but new technologies provide new solutions to overcome these obstacles. Enhanced Flight Vision Systems (EFVS) make use of infrared radiation, which can penetrate darkness and different weather conditions, providing an infrared view of the surrounding. Infrared cameras, in contrast to visual cameras, might be able to detect runways and possible obstacles even in fog. Different sensor types have different strengths and weaknesses in different weather conditions. Aerosols in the atmosphere, temperature and time of day are examples of factors that might influence the infrared radiation. Simulating the infrared transmittance through the atmosphere in different weather conditions could potentially be used to predict which sensor type would be optimal in an upcoming flight scenario. This information could be used to reduce the number of failed landing attempts by redirecting aircraft with inadequate equipment.

Saab is a world leading company within the fields of military defence and civil security. This thesis is conducted at Avionics Systems, a part of Saab group, that develops and manufactures high-quality electronics, software and mechanics for aircraft, helicopters and other applications. The work of this thesis can contribute to many fields with increased knowledge in the field of infrared radiation and sensors.

1.2 Objective

The objective of this thesis is twofold – the first is an investigation of the suitability of IR sensors in enhanced flight vision and the second is to create a simulation environment for IR imaging.

The average transmittance in different IR ranges can be used to determine what temperature differences between target and background that could be perceived by a typical state of the art IR camera. The transmitted temperature difference from ground to sensor should be compared to the NETD value of MWIR and LWIR cameras. Simulating IR propagation in different weather

conditions, with the radiative transfer code MODTRAN, could give an indication on when IR cameras are suitable for enhanced vision. The IR range should be determined and compared with the visible range, as defined by ICAO, in different atmospheric conditions in order to investigate the advantages of infrared sensors.

A simulation environment for infrared imaging of airport runways should be created from data available online. By using geographical data, airport data, weather data and the simulation software MODTRAN, a simulated IR image of a landing approach can be generated.

1.3 Delimitations

In order to carry out the project during the given time scope, several delimitations and assumptions have been made. The delimitations listed below have been considered, although further assumptions were made during the progression of the project, which have been described and motivated in Chapter 5 and 6.

- Ground classification; The ground will be classified in a limited number of classes based on their material properties.
- Modeling surface temperature; A simplified model for determining the land surface temperature will be used.
- Locations; Skavsta Airport will be used for this investigation. However, with the same approach when it comes to parameter determination, the simulation could be applied to any chosen airport.
- Climate, aerosol models and atmospheric conditions; As defined by MODTRAN.

1.4 Related Research

1.4.1 Surface temperature modelling

Land surface temperature (LST) is a crucial parameter in many fields of research and a driving force in many processes including surface energy and water balance. LST varies rapidly both spatially and temporally and qualitative measurements require extensive sampling, which would not be practically feasible when covering large areas of interest [1]. To get around this issue, scientists utilize several other approaches for LST estimation, whereof two are described briefly below. The method used in this thesis is a similar method as in the second approach below, using a fourth-degree polynomial solved iteratively for the surface temperature.

Remote sensing satellites offer the ability to estimate the LST all around the globe by measuring the radiance in different wavelengths. The method must account for the atmospheric interactions the radiation may be subject to, and also the emissivity of the surfaces [2]. Several algorithms for LST retrieval have been proposed and the article by Li et al. published in 2013 [1] reviews the status in the field. They discuss three possible ways to validate the satellite derived LST. The first one is the temperature-based method, simply comparing field-measurements with the satellite derived LST. The second one is the radiance-based method, which simulates the radiance at the

satellite position from the land surface emission spectra and measured atmospheric profiles. The third one is called the cross-validation method and compares the LST with other satellite derived LST from a reference, i.e. other well validated satellites. However, for the purpose of this thesis project, the spatial resolution obtained by remote sensing satellites is simply not sufficient.

Another approach is to use the heat flux balance and formulate a physical expression containing the surface temperature of a facet, as Maxime E. Bonjean et al. present in the article "Flight Simulator with IR and MMW Radar Image Generation Capabilities" [3]. According to the conversation of energy, the heat flux absorbed must be of the same magnitude as the heat flux lost. The surface will absorb radiation from the sun and sky, and lose energy by emitting radiation to its surroundings, to the ambient air by convection and to deeper layers of the ground by conduction. When considering these contributing factors, they formed a fourth-degree polynomial which was solved iteratively for the surface temperature.

1.4.2 Infrared sensors for enhanced vision

Maxime E. Bonjean et al. [3] have developed a real-time simulator, ARIS (Airborn Radar and Infrared Simulator), which can generate images corresponding to different sensors of interest using forward-looking infrared (FLIR) and a millimeter-wave radar (MMWR) imaging system. FLIR is a passive imaging modality which generates IR images from a viewed area based on IR radiation intensities reaching the sensor pixels. MMWR is an active image modality that operates in real time, which makes it more difficult to simulate accurately. Their investigation was undertaken to improve operational parameters of aircraft operating in adverse weather conditions. They were able to create a simulator generating real-time IR images of 3D scenes and real time MMWR images of 2D scenes. They concluded that the biggest challenge of the project was to achieve a reasonable simulation accuracy compared to a real life scenario.

N. Li et al. describes in the article "A real-time infrared imaging simulation method with physical effects modeling of infrared sensors" [4], their approach of real-time simulation of infrared imaging, including an infrared radiation characteristics model, atmospheric propagation model and infrared sensor model. To provide real-time simulations, the frame rate must be sufficient in order to avoid screen flickering. Therefore fast processing of the physics-related calculations is essential. The modeling of the infrared sensors involve physical properties in both spatial and frequency domain and they propose an enhanced image convolution method.

The use of enhanced vision systems is not only favourable on-board an aircraft, it has also been used on the runway to detect incoming aircraft. J. Miller et al. describes in the article "Runway-based infrared sensor for enhanced vision of approaching aircraft" [5], the evaluation of a fixed-field, infrared landing monitor system for aircraft detection purposes. An indium antimonide (InSb) sensor was mounted at the center of the runway of an aircraft carrier with a protective cover to avoid damage caused by aircraft wheels. The infrared imaging system was shown to perform well during approach and landing of aircraft, even under low light levels as well as in haze, smog and adverse weather conditions.

Both Bonjean et al. and Li et al. have managed to develop real-time simulators based on infrared imaging. Some compromises in accuracy of different aspects had to be made in order for the simulators to operate in real-time. The main focus was, however, not to investigate the performance of infrared sensors in poor weather conditions and a question remains to be answered – which wavelengths are optimal to detect in different weather conditions? The aim of this thesis project is therefore to more accurately examine the effect of different weather conditions on the infrared

spectrum and to determine the infrared detection range compared to visibility range.

2 Infrared radiation theory

This chapter explains the basics about infrared radiation and the way it interacts in the atmosphere and at the ground surface. The principles of modeling the atmospheric propagation as well as the surface temperature are also described.

2.1 Infrared radiation

Heat energy is stored in matter as the movement of molecules and atoms. All objects with a temperature above 0 K have some degree of molecular vibration. As the molecules collide, infrared energy is released in the form of electromagnetic radiation. The energy emitted is directly proportional to the fourth power of the temperature of an object [6].

Infrared radiation is electromagnetic radiation with wavelengths longer than visible light, and can therefore not be seen by the human eye. IR wavelengths ranges from the red end of the visible spectrum at 750 nm to 1 mm. The IR spectrum is often further divided. Table 2.1 presents a common subdivision within the range of IR [7].

Table 2.1: IR subdivisions.

Name	Abbreviation	Wavelength [µm]
Near Infrared	NIR	0.75–1.4
Short Wavelength Infrared	SWIR	1.4–3
Mid Wavelength Infrared	MWIR	3–8
Long Wavelength Infrared	LWIR	8–15
Far Infrared	FIR	15–1000

IR radiation corresponds to a significant part of the solar radiation and warms the Earth, which makes it one of the main reasons why the Earth has an environment that is suitable for life.

2.1.1 Extinction of infrared radiation

As electromagnetic radiation propagates through the atmosphere, it can interact with molecules and particles in various ways, resulting in reduced directional intensity. This reduction is called extinction and is the sum of absorption and scattering by atmospheric constituents. The remaining radiation is said to be transmitted.

The absorption of radiation means that the photon's energy is transformed into internal energy in the absorbing particle, and later on emitted as thermal radiation with longer wavelengths than the absorbed radiation. The absorption fraction is often small compared to the scattering and is usually less than 10 percent of the total extinction. For spherical particles, the absorption can be

easily calculated if the volumes and the refractive indices are known. This can be used to recognize spectral dependencies of light absorption by molecules and aerosols in the atmosphere [8].

Scattering is the process where electromagnetic radiation interacts with matter in its path, which temporarily absorbs and reradiates the energy back out with the same wavelength as the incident light in all directions. The scattering characteristics may differ as a result of the *size parameter*, *sp*. For spherical particles it is the ratio of the circumference of the particle to the wavelength of the incident radiation, $sp = 2\pi r/\lambda$, with r being the radius [9]. Mie theory offers an exact solution by solving Maxwell's equations with boundary conditions for the perturbation of the spherical particle [9]. Although Mie theory can be applicable to all sizes of spherical particles, Rayleigh scattering theory is often used when the particles are small with respect to wavelengths of light, $sp \ll 1$, due to its simplicity compared to Mie theory [10]. Mie theory is thus mostly used for particle sizes comparable to, or larger than the wavelength of the incident light.

The energy of the scattered light is a function of several variables such as size of the spherical particle and the refractive index. For small enough scattering particles, the distribution of scattered light is almost symmetric in the forward and backward directions. As the particle size increases, the scattered energy shifts more and more to the forward direction of the incident beam [11], see Figure 2.1 for illustration.

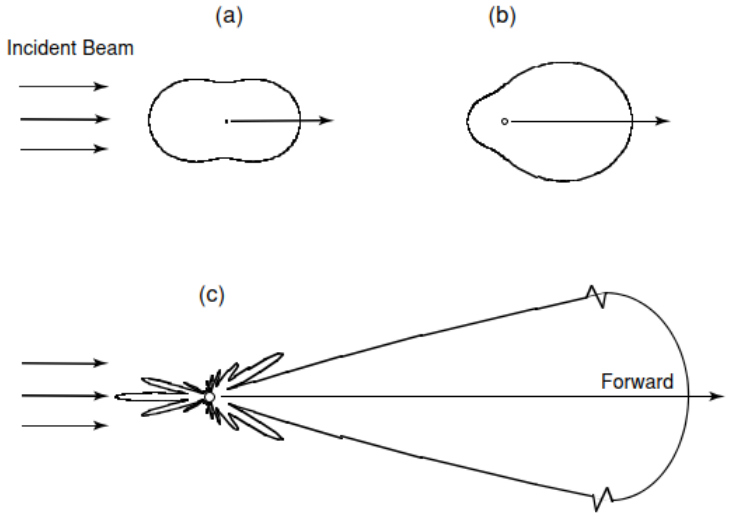

Figure 2.1: The figure shows the scattering characteristics for different sizes of particles, where (a) is a particle with radius $10^{-4}\mu m$, (b) is a particle with radius 0.1 μm and (c) is a larger particle with radius 1 μm [9].

Scattering cross section is proportional to the radiation-particle interaction probability, and represents the effective area for collision. The total scattering is proportional to the scattering cross section multiplied by the number of particles present in the medium [12].

According to Rayleigh scattering, scattering by small particles is strongly dependent on the wavelength, i.e. inversely proportional to the fourth power of the wavelength [13]. However, in the case of Mie theory, the dependence is slightly more complicated. The efficiency factors for extinction, Q_{ext}, scattering, Q_{sca}, and absorption, Q_{abs}, are the ratios of the corresponding cross sections to the geometrical cross section πr^2 of the scattering sphere. The efficiency factors with regard to *sp*

can be seen in Figure 2.2 [8]. The curves corresponding to the extinction and scattering efficiency show a combination of high and low frequency maxima and minima explained by resonance and interference phenomena respectively [14].

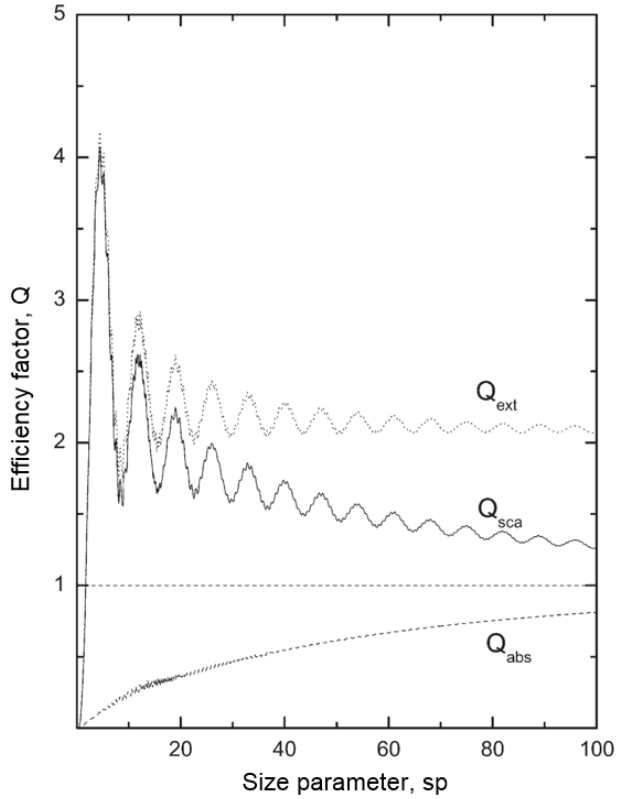

Figure 2.2: Extinction, scattering and absorption efficiency, Q_{ext}, Q_{sca} and Q_{abs} respectively, in relation to size parameter, *sp* [8].

However, particles in the atmosphere exhibit a number of different sizes and in order to provide a more realistic relationship between extinction efficiency and particle size, the effective size parameter has to be decided based on the size distribution [15]. For a distribution of particles with varying radius, the relationship appears slightly different. The distribution of varying particle sizes has a smoothing effect on the extinction curve, even for very narrow size distributions. As the distribution grows wider, the ripple structure disappears and eventually the interference structure fades away. Increased absorption also affects the appearance of the extinction in a similar way [14].

The greatest probability for scattering to occur is when the wavelength of the incident radiation is approximately equal to the radius of the particle, as seen in Figure 2.2, and as the size parameter increases, the extinction efficiency tends to approach a value of 2. Thereby, small particles with radii less than 1 µm scatter mainly in the visible portion of the spectrum, while particles of greater size scatter stronger in IR.

2.1.2 The atmosphere and atmospheric propagation of radiation

As described in Section 2.1.1, as solar radiation enters the atmosphere it is subject to three major interactions, namely, transmission, absorption and scattering. These interactions change the appearance of the radiation as it reaches the ground [6].

Radiation passing through the atmosphere may be absorbed by the molecules it consists of. As previously discussed, absorption varies depending on the molecules present, different molecules absorb radiation of different wavelengths of radiation.

The main absorbers in the atmosphere are water vapour, carbon dioxide, methane, nitrous oxide and ozone, commonly known as greenhouse gases [16]. The amount of radiation absorbed is described by the absorption coefficient, which depends on the the type of molecules [17, p. 13-14]. The incoming radiation may also be scattered by the molecules in the atmosphere. The scattering depends on the scattering coefficient of the different molecules in the atmosphere.

The fraction of the incoming radiation which is neither absorbed, nor scattered is said to be transmitted. The radiation simply propagates through the atmosphere without changing its path. Radiation scattered or emitted into the path by other surrounding molecules in the atmosphere is called path radiance and will contaminate the original radiation from the source.

The atmosphere consists of a mixture of gases surrounding the Earth, kept in place by gravity. It protects the Earth by absorbing harmful radiation such as gamma rays, x-rays and ultra violet radiation, as well as keeping the average temperature higher than it would be in the absence of the atmosphere due to the green house effect. It also evens out the temperature differences between night and day. The major components of the atmosphere are nitrogen, oxygen, water vapor, argon and carbon dioxide. The density of the gases decreases exponentially with altitude [18] [17, p. 9-10].

The different molecules in the atmosphere have different properties and they therefore interact differently with the incoming radiation. The various molecules selectively absorbs radiation of different wavelengths in the spectrum. This means that not all wavelengths pass through the atmosphere and eventually reach the surface of the Earth. The wavelengths that do however, are commonly referred to as the atmospheric window. This is the range of wavelengths that more easily pass through the atmosphere with little attenuation [17, p. 39] [19], and is illustrated in Figure 2.3.

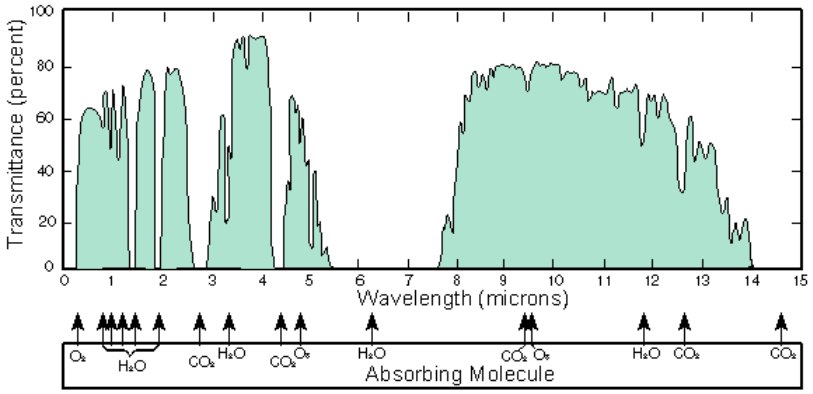

Figure 2.3: Atmospheric window in the IR range. The transmission of different wavelengths are illustrated as well as the absorbing molecules.

2.1.3 Weather effects on infrared radiation

The definition of weather is commonly known as the state of the atmosphere. Temperature, pressure, humidity, precipitation, solar radiation and wind are influencing factors. Since the weather changes the properties of the atmosphere, the atmospheric window will also vary and therefore different IR wavelengths and amounts of radiation will be attenuated.

The scattering in different parts of the spectrum depends largely on the size distribution of the aerosols and droplets in the atmosphere [20]. As mentioned in Section 2.1.1, for spherical particles it is correlated to the ratio of the circumference to the wavelength of the incident radiation. In reality, the particles present in the atmosphere have different sizes and scattering therefore occurs for many wavelengths at the same time. The liquid water content is also an influencing factor of attenuation [15].

Generally visibility in IR is better at low absolute humidity, for example during winter, and worse in the tropics where humidity is high. Different types of aerosol also affect the detection range in IR, mostly depending of the size distribution and concentration of particles [15].

Radiative properties of fog

For fog to form, the air must be saturated with water vapor. This means that the relative humidity is close to 100 %. There must also be a sufficient amount of condensation nuclei present (microscopic particles in the air). A foggy atmosphere is a mixture of gas and particles [21].

There are two types of fog formation processes: one is the mixing of two air masses with different temperature or humidity, called advective fog, the other is called radiative fog which is the result of radiative cooling close to the dew point. Advective fog is most common around coastal regions. The fog forms when warm and moist air moves over a cooler surface, the ocean for instance. The surface cools the air to the dew point, which results in fog [22]. Radiative fog is the most common type of fog. For radiative fog to form, clear skies, moisture in the air and light winds are required. The fog is formed when heat from the surface radiates back to the air close to the surface, which

saturates it [22]. The light wind brings the fog to higher levels in the atmosphere, which creates a thicker layer of fog.

For all wavelengths less than 1 cm, the propagation of electromagnetic radiation is impaired by fog particles due to scattering and absorption. Scattering is the main process in foggy conditions. The micro-physical structure of the aerosols determines the amount of scattering and absorption. The main parameters of aerosols to consider are the chemical composition of condensation nuclei, size distribution and liquid water content. The typical size of aerosols vary from 10^{-4} µm to 1 µm in radius, but in fog the particles can grow to 30 µm in radius [15].

Studies have shown that developing fog has a droplet concentration of 100-200 particles per cm^3 with a radius of 1-10 µm, and a mean radius of 2-4 µm. When the fog thickens, the droplet concentration drastically diminishes and the mean radius of the particles increases to 6-10 µm [21]. The radiative fog is characterized by a narrow size distribution, whereas the advective fog is characterized by a broader size distribution with larger particles.

2.1.4 Surface interaction

The radiation reaching Earth's surface originates from different sources – there are solar and sky radiance, but also radiation scattered or emitted by the atmosphere and from other nearby objects. The radiation reaching the surface is either directly reflected or absorbed, since the surface is opaque, no transmission is possible [3]. An object's or material's ability to reflect light is referred to as albedo. Snow and ice for example have high albedo and reflect most of the incident radiation, while heavy vegetation and oceans have low albedo, meaning that most of the radiation is absorbed [23]. The absorbed radiation contributes to the heating of the surface. There is also a heat exchange between the surface and underlying layers resulting in temperature changes at the surface, known as conduction, as well as heat transfer between the surface and the ambient air which is called convection [3]. The surface interactions, as well as the atmospheric interactions, are illustrated in Figure 2.4.

As previously discussed, the emitted radiation corresponds to the temperature of the surface. At thermal equilibrium, the absorbed energy is transformed to heat energy and later emitted as thermal radiation as stated by Kirchoff's law [24, p. 26]. The emittance of a perfect emitter, also called blackbody can be described by Planck's law [24, p. 8], however most objects are not perfect emitters and will reflect a portion of the incident radiation. The emissivity of a material can vary with respect to wavelength and temperature [24, p. 23] [6].

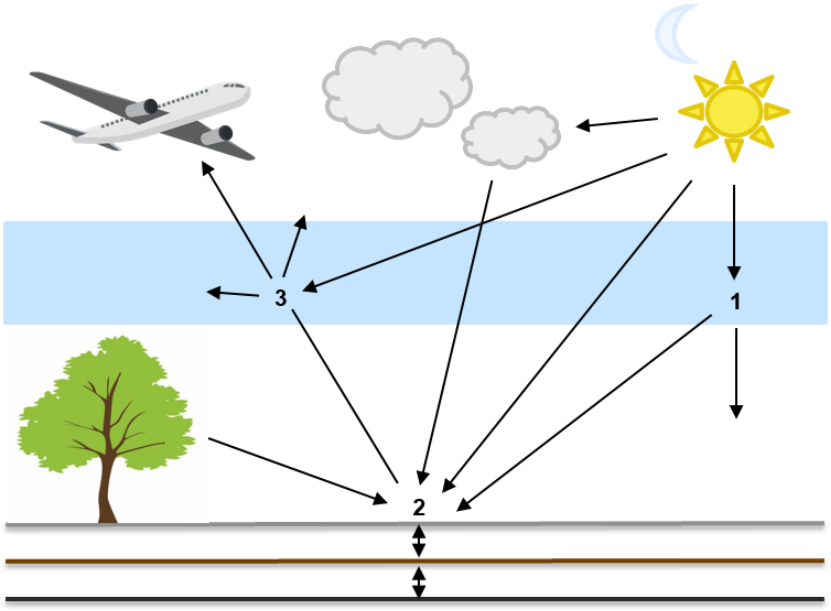

Figure 2.4: The figure illustrates how radiation interacts in the atmosphere as well as at the ground surface. 1) Solar radiation is either transmitted, scattered or absorbed. The absorbed radiation is later emitted as thermal radiation. 2) Radiation from the sun strikes the surface, but also radiation scattered or emitted by the atmosphere and from other nearby objects. The radiation reaching the surface is either directly reflected or absorbed. 3) Radiation emitted or reflected by the surface interacts in the atmosphere in the same way as the incoming solar radiation, i.e. by transmission, scattering or absorption.

2.2 Modeling interactions of infrared radiation

This section describes the modeling of atmospheric propagation and also a simplified model to determine temperature of different surface types.

2.2.1 Modeling atmospheric propagation of radiation

As mentioned in the previous section, the incident radiation toward the surface of the Earth originates from different sources. There are solar and sky radiation, as well as radiation emitted and scattered from other nearby objects. The incoming radiation suffers reductions due to different atmospheric interactions. The total reduction is referred to as extinction and is proportional to the incoming radiation, the density of the atmosphere along the path, to thermally emitted radiation as well as the distance travelled. The extinction factor, β, can be expressed as the sum of the scattering, σ, and the absorption, α [17, p. 3].

$$\beta = \sigma + \alpha \tag{2.1}$$

The remaining radiation, reaching the target surface, corresponds to the transmission. The trans-

mittance factor, τ, depends upon the path length, r, and the extinction factor [17, p. 6].

$$\tau = e^{\beta r} \tag{2.2}$$

The radiation striking the Earth's surface is the sum of the transmitted radiation from all the contributing sources. The incident radiation is either reflected, ρ, or absorbed, α, by the surface.

$$\rho + \alpha = 1 \tag{2.3}$$

As any object with internal heat, the surface will emit thermal radiation. The radiant exitance, M, is described by Planck's law of blackbody radiation [24, p. 8-9]

$$M(\lambda, T) = \frac{2\pi c^2 h}{\lambda^5 (e^{hc/k\lambda T} - 1)} \left[\frac{W}{m^2}\right] \tag{2.4}$$

where c is the speed of light in vacuum, h is Planck's constant, T is the temperature of the object's surface expressed in Kelvins and k is Boltzmann's constant. The determination of the surface temperature is challenging, since many factors have to be considered. The calculation of the surface temperature will be covered later on in this section. M is the total exitance from an object, emitted in all directions, for an isotropic radiator the radiance at a specific direction, at a solid angle, is [24, p. 10]

$$L(\lambda, T) = \frac{1}{\pi} M(\lambda, T) \left[\frac{W}{sr \cdot m^2}\right]. \tag{2.5}$$

The exitance and radiance described above assume the emitting material to be a blackbody, a perfect emitter. If a material is not a perfect emitter the emissivity, ϵ, describes the effectivity of emittance compared to a blackbody at the same temperature. The radiance from the Earth's surface, denoted by L_{sur}, can be expressed as the radiance from a blackbody, L_{BB}, times the emissivity [6]

$$L_{sur}(\lambda, T) = \epsilon L_{BB}(\lambda, T). \tag{2.6}$$

Through the assumption of thermal equilibrium at the surface, the absorbed energy will be emitted as thermal radiation according to Kirchoff's law [24, p. 26] [6], and therefore

$$\epsilon = \alpha. \tag{2.7}$$

However, the absorptivity of many real surfaces are insensitive to temperature and wavelength and the assumption of absorptivity and emissivity being equal can thus be made even without thermal equilibrium [6]. Equation 2.7 together with 2.3 states the following relation

$$\rho + \epsilon = 1. \tag{2.8}$$

The total radiation leaving the surface is thus the sum of the reflected and the emitted radiation. This radiation is once again subject to the atmospheric interactions before eventually reaching the observer. Path radiance is also introduced along the way, i.e. radiation scattered or emitted into the path by other surrounding molecules in the atmosphere, and will also be indistinguishable from light originating from the surface. The detected radiance is therefore the sum of the radiation from the target surface, transmitted through the atmosphere, and the path radiance.

$$L_{obs}(\lambda) = \tau L_{sur}(\lambda) + L_{path}(\lambda) \tag{2.9}$$

Where L_{sur} is the radiance coming from the surface transmitted by a factor, τ, and L_{path} is the radiance scattered into the path. L_{obs} is thus the radiance detected by an sensor at a certain viewing angle.

2.2.2 Modeling surface temperature

To be able to properly calculate the exitance and radiance from a surface (Equation 2.4 and 2.5), the temperature must be determined. Modeling the surface temperature, T_s, is a complex problem. The conservation of energy predicates that the energy absorbed must be equal to the energy lost to the surroundings. In other words, the incident radiation from the sun and sky absorbed by the surface is equal to the energy lost by radiation, convection and conduction. The radiation loss corresponds to the thermal radiation emitted. Convection is the heat exchange with the surrounding air, as circulations of the air occur due to the difference in density of warm and cool air. Conduction is heat exchange between two objects in contact with each other when there is a difference in temperature, in this case the land surface and the underlying layers of the ground. The heat flux balance can therefore be written as follows [3]

$$E_{abs} = M_{lost} \tag{2.10}$$

where

$$M_{lost} = M_{rad} + M_{conv} + M_{cond} \tag{2.11}$$

with E representing irradiance and M representing exitance, both expressed in the units of $[W/m^2]$. The different components of Equation 2.11 is given by Equations 2.12 through 2.16 [3]. The incident absorbed radiation is described by

$$E_{abs} = \alpha E_{in} \tag{2.12}$$

with α being the absorptivity of the surface and E_{in} the incident radiation striking the surface.

The radiative loss is the product of the surface emissivity, ϵ, the Stefan-Boltzmann constant, σ_e, and the (yet unknown) surface temperature, T_s, raised to the fourth power.

$$M_{rad} = \epsilon \sigma_e {T_s}^4 \tag{2.13}$$

The convected exitance is the product of the convective heat transfer coefficient, h_c, and the temperature difference between the surface and the ambient air

$$M_{conv} = h_c(T_s - T_{amb}) \tag{2.14}$$

where h_c for air is given as an expression of the relative speed difference between the object surface and the air, i.e. the wind speed v.

$$h_c = 10.45 - v + 10v^{1/2} \tag{2.15}$$

The wind speed is assumed to be a laminar flow over a plane surface. The conductive loss is given by the following relation

$$M_{cond} = \frac{\kappa}{\Delta x}(T_s - T_{layer}) \tag{2.16}$$

where κ is the thermal conductivity of the surface material and T_{layer} is the temperature at depth Δx. In Equation 2.16, κ is assumed to be constant in Δx.

Using Equations 2.12 to 2.16, Equation 2.10 can be rewritten as

$$\alpha E_{in} = \epsilon\sigma_e {T_s}^4 + h_c(T_s - T_{amb}) + \frac{\kappa}{\Delta x}(T_s - T_{layer}) \tag{2.17}$$

which can be solved for T_s with numerical methods.

3 Flight systems and sensors

In order to increase the safety of flight operations, different electronic systems and sensors have been developed throughout the years. This chapter covers the basics about the ground based instrument landing system as well as the airborne enhanced flight vision system and more in depth about infrared sensors.

3.1 Instrument landing system

The approach and landing of an aircraft can be a difficult task if the visibility is reduced. An instrument landing system (ILS) is a ground based system, transmitting radio signals to provide horizontal and vertical guidance together with ground based lights along the runway. The system consists of a *localizer*, which provides information of the horizontal position relative to the runway and a *glide slope*, which provides vertical guidance so that the aircraft follows the right incident angle, normally around 3° relative the horizontal plane, see Figure 3.1. Some systems also include markers operating at a certain frequency, which indicates the distance from the runway [25].

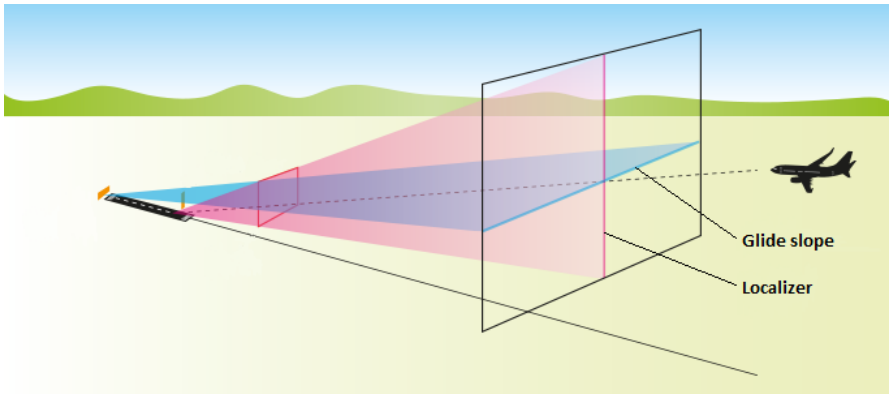

Figure 3.1: Illustration of ILS.

There are three main categories of ILS's, CAT I/II/III, based on the decision height and the visibility range along the runway, see Table 3.1 with definitions according to International Civil Aviation Organization (ICAO). CAT III is further divided into three subcategories. As an airplane descends for landing, the decision height is an important concept. It is the height at which the pilot must have gained the visual reference required for the landing approach. If the required visual reference has not been established, a missed approach must be initiated, i.e. the approach must be aborted and further guidance must be initiated by air traffic control [26].

Approval for different levels of ILS operations is dependent not only on the airport system but also the aircraft equipment and flight crew qualifications. Category III operations require an automatic landing system since visibility is not sufficient to perform a manual landing.

ILS require extensive maintenance and calibration in order to ensure high accuracy and is therefore very expensive. Some airports have therefore chosen to focus on other systems such as global positioning system (GPS) and microwave landing systems (MLS). However, this readjustment increases the demand on the aircraft and the equipment they carry [27].

Table 3.1: Categories of ILS, definition according to ICAO, stating minimal decision height (DH) and runway visibility range (RVR) [28].

CAT	DH	RVR
I	$>$ 200 ft (60 m)	1800 ft (550 m)
II	$>$ 100 ft (30 m)	1200 ft (350 m)
IIIa	no DH or $<$ 100 ft (30 m)	700 ft (200 m)
IIIb	no DH or $<$ 50 ft (15 m)	150 ft (50 m)
IIIc	no DH	no limit

3.2 Enhanced flight vision system

Visibility is one of the primary factors influencing the safety of flight operations. An enhanced flight vision system (EFVS) is an airborne system of forward looking imaging sensors such as IR and radar to provide the pilot with an image of the scene, even in bad weather and darkness when human vision is insufficient [29]. The operating wavelengths of IR and radar have better weather penetrating properties than visual light and will therefore provide better understanding of the surroundings. The image is displayed conformal to the scene, usually on a so called head-up display (HUD), see Figure 3.2. A HUD is a transparent display overlapping data in the pilot's line of vision.

Figure 3.2: Illustration of HUD with EFVS in limited visual conditions [30]

From March 2017, the FAA (Federal Aviation Administration) decided upon a rule [31, §91.176] which states that qualified pilots are allowed to use EFVS in lieu of natural vision, in order

to descend below decision height and to touch down even when visibility is limited. With this regulation, EFVS might reduce the risk of failed landing attempts and will thereby increase the safety of landings and capacity of airports in unfavourable weather conditions [29].

The combination of different types of sensors, for example IR sensors and MMWR can provide an image of the outside scene even in poor visibility conditions. The EFVS usually includes several different sensors and cameras. Examples of techniques that might be suitable for EFVS purposes are listed below.

- FLIR: FLIR cameras are traditionally of two types: the MWIR band camera, 3-5 μm, or the LWIR band camera, 8-14 μm. These sensors will be described more in depth in Section 3.3.
- SWIR: The SWIR camera, operating in 0.9-1.7 μm, is a relatively new technique, made possible by the development of Indium Gallium Arsenide (InGaAs) sensors. SWIR share many properties with visible light, which makes it possible to see shadows and the resolution is comparable to visible images. SWIR cameras can operate in the dark by utilizing the night sky radiance or in the absence of such, illuminating the scene with an eye safe laser in the SWIR band [32]. SWIR also has the advantage of penetrating atmospheric haze and smog, where visible light is scattered [33]. However, when the particle size increases, even SWIR is attenuated and the imaging ability becomes limited [34].
- PMMW: A passive millimeter wave (PMMW) camera is a promising technique for EFVS. It operates in the 1-4 mm wave band. The principle is the same as for FLIR, the blackbody radiation emitted from objects is captured through a lens and focused on to a sensor. The cameras are very large since the energies involved at millimetric wavelengths are much smaller than for thermal IR. PMMW cameras have shown good performance in adverse weather conditions although the resolution is low [35].
- MMWR: Pulses of millimeter waves are emitted, and later reflected against a surface or target, back to the receiver. The reflected echo is then used to determine the distance between the sensor and the target and to create a two-dimensional image. The radar image is generated based on backscatter which is a function of the incident angle. The capability to penetrate adverse weather such as clouds, fog and rain is an advantage of MMWR. A disadvantage is that a lot of computational power is required for image formation since there is no lens involved, the resolution is similar to that of PMMW [36].
- LiDAR: The technology of LiDAR is based on the same principle as radar, with the difference that laser light pulses of wavelengths around 1 μm are emitted instead of radio waves. This technique is fundamental in self-driving cars, in order to localize objects nearby the vehicle [37]. The operating range is strongly dependent on the laser power and typically less than 1 km, which is usually enough for cars, however a little short in the context of EFVS. Due to shorter wavelengths than radar, the spatial resolution is increased, however the weather penetrating ability is decreased [38].

3.3 Infrared sensors and systems

Infrared imaging is achieved by converting infrared radiation to a visual image with a camera sensitive to infrared wavelengths. The temperature differences across a scene is what is actually imaged. An infrared camera mainly includes an optical system, a detector system in the form of a focal plane array (FPA), a detector cooling system and a signal processing system to display

images [39], see Figure 3.3. The FPA is made of pixels in micrometer sizes and the resolution can be up to 1024 x 1024 pixels. The major part of the detectors are not sensitive for the full IR range, therefore the response curve of a detector is more narrow. Consequently, a detector sensitive for a certain IR range is suitable in situations and applications where the infrared radiation span matches that of the detector.

The infrared radiation coming from a radiating object must pass through the atmosphere before it reaches the camera. It is therefore important that the detector's response curve matches the atmospheric window. There are three main operational bands for IR detectors: the short wavelength band, 1-3 µm; the medium wavelength band, 3-5 µm; and the long wavelength band, 8-14 µm. In the 5-8 µm band, the spectral absorption of the atmosphere is too large and can therefore not be used for imaging. There are several different types of detectors that are suitable for these wavelengths, respectively [40].

There are similarities in the design of the optics of infrared cameras and visual cameras. In visible light cameras, glass is used in the optics. This is however not possible for infrared cameras, since infrared radiation is not transmitted through glass well enough. Materials that are opaque to visible wavelengths, might be transparent to infrared wavelengths. An infrared camera lens is typically made of silicon or germanium materials [41].

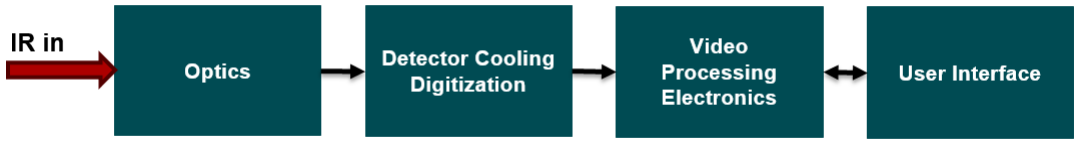

Figure 3.3: Flow chart of detector system.

There are thermal and quantum type detectors, which operate in different ways. A microbolometer is a thermal detector where the FPAs are made of metal or semiconducting materials. IR radiation heats the material and thus changes its resistance, which is in turn converted to a temperature. The microbolometer does not need to be cooled, however this type of detector is not so sensitive and the response time is slow, which is why quantum detectors are required for more advanced applications [42]. Quantum detectors have a fast response time and high detection performance [43]. Quantum detectors work based on the principle of photoelectric effect. The materials in quantum detectors absorb photons from IR radiation which leaves electrons in a higher energy state. This generates a change in conductivity, voltage or current. Quantum detectors must be cooled in order to obtain accurate measurements. The response curves of quantum detectors vary with wavelength [41]. In Table 3.2 below, different common detector materials can be seen.

Table 3.2: Common detector types and materials [41].

Detector type/material	Operation	Operating temperature
Microbolometer	Broadband detector	Uncooled
HgCdTe	SWIR photon detector	200 K
HgCdTe	LWIR photon detector	77 K
InSb	MWIR photon detector	77 K
PtSi	MWIR photon detector	77 K
QWIP	LWIR photon detector	70 K

3.3.1 Signal Transfer Function

In order to generate an image based on the signal input of an infrared sensor, a Signal Transfer Function (SiTF) is needed. SiTF measures the response of a camera, the signal output versus the signal input [44]. The brightness of an object viewed in the camera, the output signal, varies with the objects temperature, the input signal. SiTF measures the amount of signal change per change in temperature. The change in temperature is defined as the temperature difference between an object and background. The SiTF is generated by evaluating known temperature differences and plotting them against grayscale values or digital units, see Figure 3.4.

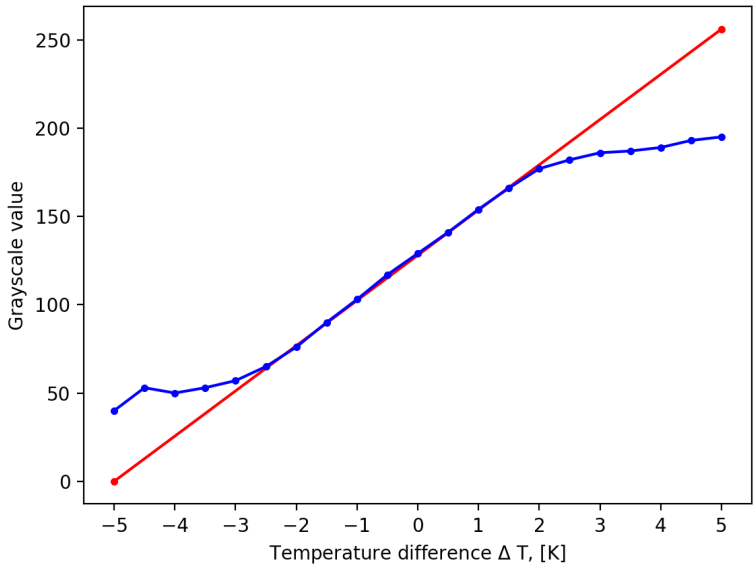

Figure 3.4: Example of a SiTF for an IR camera. The blue line corresponds to a typical measured response curve, S-curve. The red line shows a straight line approximation of the S-curve, the SiTF, which is valid for the center region.

The response curve is typically referred to as an S-curve. In the lower left of the curve, the flat region, there is not enough temperature change to stimulate the camera. In the upper right, the

response of the camera is flattened again. This is because of the fact that there is too much temperature change which saturates the camera. The middle region, the linear part, is the most important part. From the values in the S-curve, it is possible to approximate a line in the center region, $y = kx + m$, which gives a value of change of digital unit, [DU], per degree, [K]. This is the SiTF.

3.3.2 Noise Equivalent Temperature Difference

Noise Equivalent Temperature Difference (NETD) is also sometimes referred to as thermal contrast. Noise is the variation in signal from a sensor, that is not due to the items appearing in the field of view of an infrared camera. Noise limits the smallest detectable temperature difference that can be resolved. With a low noise level, smaller temperature differences can be measured. The more noise there is, the higher the NETD value of the detector [45].

The NETD value of a infrared camera is measured by pointing the camera at a temperature controlled blackbody. The noisy image produced is used to find the standard deviation, σ, of all pixel values [45]. The NETD can be calculated as follows:

$$NETD = \frac{\sigma}{SiTF} \tag{3.1}$$

The NETD value is typically expressed in milli-Kelvin, [mK], since it is calculated from the standard deviation, σ [DU], and the response of the camera, SiTF [DU/K].

4 Software and data

A great part of this study involved searching for and investigating different options of software and appropriate data. This chapter briefly presents the software and data sources used.

4.1 Geographical data

In order to properly classify the ground, geographical maps with different properties were used and combined. Below are brief descriptions of the geographical data used for this purpose.

4.1.1 OpenStreetMap

OpenStreetMap creates and provides free geographic data. The OpenStreetMap project is operated by the OpenStreetMap foundation, which is an international non-profit organization. The objective of the project is to encourage the growth and development of geospatial data and to make it available for everyone. Most maps have legal and technical restrictions, which makes it difficult for people to use them in a creative ways. The OpenStreetMap project is crowdsourced data and is made available under the Open Database License [46].

The data used for OpenStreetMap is collected by volunteers and then added to the OpenStreetMap database. Also, satellite images and other forms of data have been obtained from commercial and governmental sources. Editing of maps can be done with different web browser editors available online.

OpenStreetMap uses a topological data structure, with four different core elements. These are nodes, ways, relations and tags. Nodes are coordinate points (latitude and longitude) that represent a geographic position. Nodes are present in ways and they are also used to map points that do not have a size, like the location of a mountain peak. The ways are represented by several nodes which in turn creates a line structure or a polygon area if they form a closed loop. The line structures can represent highways, rivers etc., and the areas can represent forests, meadows or buildings etc. Relations consists of list of nodes, ways and other relations. Relations are used to describe geographic relationships between objects. A member of a relation can have a role which describes the part that a particular feature plays within a relation. Tags are string attributes that can be used to store metadata about objects in the map, for example type, name and physical properties. The tags are always attached to either a node, way or relation. There is a dictionary for which tags that are commonly used. In June 2017, there were over 89 million different tags in use. Figure 4.1 below is an example of the data structure in OpenStreetMap, showing the connection of the different core elements.

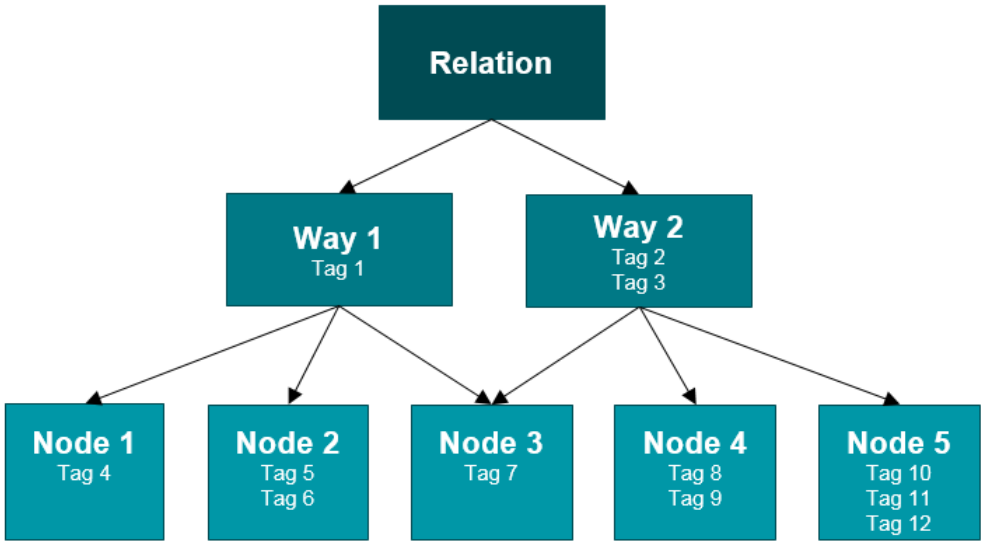

Figure 4.1: Example of the data structure in OpenStreetMap.

4.1.2 Satellite imagery

Satellite imagery are images of the Earth gathered by imaging satellites, usually operated by governments and businesses. These images are sold by licensing them to businesses such as Google Maps. There are several satellites in operation today, collecting satellite imagery. Multiple websites from agencies around the world equip users with high quality satellite imagery.

Satellite images obtained by NASA are available for free to the public, published by NASA Earth Observatory. Many countries have some kind of satellite imaging program. In Europe, ERS and Envisat satellites were launched, carrying several types of sensors. Satellite imagery became more available during early 21st century. This is when affordable and user friendly software became available to access satellite imagery databases.

Satellite images are an important factor in many applications today, for example in meteorology, agriculture, forestry, regional planning and warfare to name a few. Images can be collected in the visible wavelength spectrum and in other spectra. There are also elevation maps, which are created from radar images.

Satellite imagery by remote sensing involve four different types of resolution; spatial, spectral, temporal and radiometric. The following definitions are made by Campell [47].

- Spatial resolution: Depends on the sensor's field of view, the pixel size represents the surface area of the ground.
- Spectral resolution: The size of the wavelength interval (part of the electromagnetic spectrum) and the number of intervals that the sensor can measure.
- Temporal resolution: The amount of time, in days, that passes between two image collection periods for a given location.

- Radiometric resolution: The capability of the imaging sensor to record different levels of brightness (which generates contrast).

The resolution of satellite images is quite different depending on the sensor properties and the altitude of the sensor position. The resolution can vary from 0.41 m up to 30 meters. Aerial photography achieves higher resolution and works as a supplement to satellite imagery. Raster and vector data can also be combined with satellite imagery in a Geographic Information System (GIS), given that the imagery is spatially correct and can coordinate properly with other data sets.

4.2 Material specific data

Different materials have varying emissivity, ϵ, i.e. efficiency in emitting radiation, and must therefore be taken into account in the calculation of surface temperature. Generally, dark coloured and rough surfaces have higher emissivity compared to light and polished surfaces. The emissivities for some relevant materials can be seen in Table 4.1 below.

Table 4.1: The emissivity, ϵ, coefficients for some relevant materials [48] [49] [50].

Material	ϵ
Asphalt	0.93
Grass (dry yellow)	0.95
Grass (green)	0.98
Water	0.95
Snow	0.80
Forest	0.98

The emissivity is however also dependent on viewing angle, wavelength and the temperature of the surface or object. The above stated values are assumed to be a good overall approximation.

In order to calculate the heat transfer by conduction, the thermal conductivity of the ground material must be known. The thermal conductivity, κ, of some common ground materials are presented in Table 4.2 below.

Table 4.2: Thermal conductivity for some relevant materials [51] [52].

Material	κ [W/(mK)]
Asphalt	0.75
Soil (dry)	0.36
Soil (moist)	1.6

4.3 Weather data

The weather data used in the surface temperature model and thus in the simulation, have been collected from the Swedish Meteorological and Hydrological Institute (SMHI). Many different weather

parameters are available for download, from the last hour ranging back to the beginning of measurement documentation. The relevant parameters used in this study will be presented below.

Solar irradiance is the incident radiation energy from the entire sky, striking a horizontal area, summed up over the wavelength interval 0.28 - 4 µm. The solar irradiance is measured by a pyranometer in the unit W/m^2 [53].

Hourly values of wind speed are measured by an anemometer and averaged over 10 minutes every hour. Practically all measurements are performed at automatic stations (with only a few exceptions, with manual measurements), from a height of 10 meters above ground. Wind speed is presented in the unit m/s [54].

Temperature data are available in many different forms, relevant to this study are however only hourly and daily averaged values. Temperatures are measured automatically by electronic resistance thermometers in the unit °C. To obtain as uniform measurements as possible, the temperature is measured in an open flat surface area, at a height of $1.5 - 2$ meters above the ground. The thermometer is also shielded from direct sun light and precipitation [55].

4.4 Radiative transfer software

4.4.1 MODTRAN

As previously discussed in Section 2.1 infrared radiation is subject to various interactions when propagating through the atmosphere. MODTRAN (MODerate resolution atmospheric TRANsmission) is a radiative transfer software designed for modelling complex atmospheric transmittance and radiance calculations given a specific path [56]. The calculation takes into account molecular and aerosol absorption and scattering, atmospheric self-emission and path radiance etc. The model operates over the ultraviolet through long infrared wavelengths and offers a resolution of 0.1 cm^{-1}.

MODTRAN makes it possible to model the atmosphere with a variety of different atmospheric conditions. It has six different standard climate models, see Table 4.3, corresponding to different seasons and geographical locations with a standard ground temperature. The climate models have defined pressure and temperature profiles for more than 50 atmospheric layers, from sea level to an altitude of 120 km. The ratio of 25 different atmospheric species are defined for every layer. MODTRAN also contains six different aerosol models, see Table 4.4, which can be paired with all climate models. The aerosol models define the atmospheric properties in the boundary layer and are affected by properties such as earth surface and weather. It is also possible for the user to define climate and aerosol models from own meteorological measurements. Different cloud models and different rain rates can be set. In addition to these standard settings, several other parameters can be altered, for example geometry of sensor position, length of atmospheric path, surface types and temperature, and emissivity of different surfaces.

Table 4.3: Standard climate models and corresponding ground temperature in MODTRAN.

Climate model	Ground temp [K]
Tropical	299.7
Midlatitude summer	294.2
Midlatitude winter	272.2
Subarctic summer	287.2
Subarctic winter	257.2
US Standard	288.2
User defined	User defined

Table 4.4: Standard aerosol models in MODTRAN.

Aerosol model	Default visibility [km]
Rural	23
Maritime	23
Desert	Based on windspeed
Advective fog	0.2
Radiative fog	0.5
User defined	-

The physics behind the radiation transport make it possible to accurately model a vertically stratified and horizontally homogeneous atmosphere, based on a local earth radius. Both molecules and particles are modeled in the atmosphere through vertical profiles. Their concentrations can be defined either by the user or by using built-in models. In MODTRAN, the radiative transfer equation is solved. The most relevant parts of the physics which the MODTRAN code is based on, can be found in the Appendix. The radiative transfer function includes the effects of molecular and particulate absorption/emission and scattering, the reflections and emission from different types of surfaces, solar/lunar illumination, and spherical refraction. The underlying physics and algorithms used in MODTRAN are well established and extensively validated.

Several different outputs can be obtained from MODTRAN; narrow spectral band direct and diffuse transmittances, path component and total radiances, transmitted and top-of-atmosphere solar/lunar irradiances, horizontal fluxes, cooling rates, and more. Further information regarding the function and performance of MODTRAN can be found in its documentation [57].

Optical properties of aerosol models

The following section briefly describes the use of aersol models in MODTRAN, based on the work of Eric P. Shettle and Robert W. Fenn [21].

The propagation of infrared wavelengths through the atmosphere is affected by absorption and scattering by molecules and particles in the air. Haze, dust, fog and cloud droplets are examples of particles affecting the propagation. Close to the earth's surface, in the boundary layer which

is about 2 km thick, the scattering and absorption by aerosols are significant, especially when the visibility is low.

The aerosol particles in the atmosphere can vary remarkably in their concentration, size and composition, and therefore in what influence they have on propagation of infrared radiation. Models for atmospheric aerosols are necessary in order to make estimates of the transmittance, light scattering, radiance or other atmospheric properties and effects. In the boundary layer, these models define an average type of aerosol whose concentration can be defined based on surface visibility.

Extensive measurements of aerosol concentrations, their size distribution and optical properties have been made and lay the ground for these type of models. The optical properties of the models are defined for a wavelength span of 0.2-40 µm and take the relative humidity into consideration.

The size distributions, n(r), for different aerosol models can be presented as one or the sum of two log-normal distributions:

$$n(r) = \frac{dN(r)}{dr} = \sum_{i=1}^{2} \left(\frac{N_i}{ln(10) \cdot r \cdot \sigma_i \sqrt{2\pi}} \right) exp\left[- \frac{(log(r) - log(r_i))^2}{2\sigma_i^2} \right] \tag{4.1}$$

N(r) is the density of particles with radius r, σ is the standard deviation, N_i is the number density with mode radius r_i. This type of size distribution considers the versatile nature of the aerosols.

There are five different standard aerosol models for the atmospheric conditions in the boundary layer, as mentioned in Section 4.4.1. The size distribution and the refractive index of the particles are varied between the different models. If the visibility is altered, the size distribution will be re-normalized to give a correct extinction factor. The visual meteorological range, V, is defined at a wavelength of 550 nm and is expressed as follows:

$$V = \frac{1}{\sigma} \, ln\left(\frac{1}{\epsilon}\right) = \frac{3.912}{\sigma} \tag{4.2}$$

ϵ is the threshold contrast at 2 % and $\sigma = \sigma_{molecular} + \sigma_{aerosol}$ is the total extinction.

When the relative humidity in the air is increased, water vapour condenses onto the aerosols which makes them increase in size. The composition and the refractive index of the particles are changed. This generates a change on the absorption and scattering of light, which will be changed corresponding to the increase of the humidity. The change in particle size depends on the relative humidity.

The fog models in MODTRAN are presented by Silverman and Sprague in their work and represent the range of measured size distributions corresponding to advective and radiative fog, respectively [58]. A modified gamma distribution is used to describe the size distributions.

To calculate the scattering and absorption coefficients of different aerosols, based on size distribution and refractive index, Mie theory is used. Particles are assumed to be spherical, which in general is not the case. Liquid aerosols are often spherical, whereas dry particles generally have irregular shapes. However, irregularly shaped particles scatter light in a similar way to spherically shaped particles.

Atmosphere Generator Toolkit

The Atmosphere Generator Toolkit (AGT) is an extension to MODTRAN, which makes it possible for the user to generate customized atmospheres. The following inputs are needed; latitude, longitude, date and time. An atmospheric profile is generated for a desired location at a defined time of the year, based on averaged historical data.

The data needed comes from the National Oceanic and Atmospheric Administration (NOAA) database. They provide long-term time-averaged data from across the globe. Altitude dependent pressures, temperatures and relative humidities have been collected by radiosondes on a 2.5 latitude by 2.5 degree longitude grid. The data has been collected four times a day which covers the globe at 6 hour intervals averaged from 1981-2010.

5 Method - Part I: Infrared transmittance in different weather conditions

The following chapter presents the approach of the analysis of infrared propagation in the atmosphere with regard to different weather models. The investigated conditions are defined and the simulations performed by MODTRAN is described. The results from this investigation will be presented in Chapter 7.

5.1 Investigated weather conditions

The simulations of different atmospheric compositions have been performed for a climate corresponding to the location of Skavsta Airport, in most cases during winter time. The background atmospheric condition was generated using the AGT, described in Section 4.4.1. Different weather conditions according to MODTRAN definitions have been investigated. The weather conditions consider different atmospheric compositions with varying attenuation. MODTRAN offers several aerosol models with the possibility to set the visibility, i.e. surface meteorological range. The visibility was, in most cases, set according to the ICAO categories, see Table 3.1. A summary of the simulated weather conditions are presented in Table 5.1 and further described in the following sections.

Table 5.1: Investigated weather conditions simulated with MODTRAN with chosen aerosol models and investigated visibility.

Case	Weather condition	Aerosol model	Visibility [km]
1	Clear weather	Rural, urban, maritime	23, 5, 23
2	Radiative fog	Radiative fog	0.55, 0.35, 0.20, 0.05
3	Advective fog	Advective fog	0.55, 0.35, 0.20, 0.05
4	Rain	Rural + diff. rain models	Determined by rain model

5.1.1 Clear weather

Simulations were performed with an AGT generated atmosphere, corresponding to Skavsta Airport in January 1st at noon, and rural aerosol with default visibility 23 km. No clouds, fog or rain was added to the model in order to determine the transmission in clear visibility weather. The sensor position was defined by altitude, 60 m and 520 m, and zenith angle, 93°.

In order to compare the transmission in summer and winter time, the same simulation was performed, only this time with an AGT generated atmosphere corresponding to 19th of July. Sensor altitude was set to 60 m for this simulation.

A comparison between three different aerosol models with default visibility was performed. The

same AGT generated atmosphere for winter time was used together with MODTRAN defined rural, urban and maritime aerosol model. Default visibilities were 23 km for rural and maritime and 5 km for urban aerosol. The sensor position was defined by an altitude of 520 m and a zenith angle of 93°.

5.1.2 Radiative fog

Radiative fog was investigated by simulating the AGT generated atmosphere for winter time together with the radiative fog aerosol model. A summer atmosphere was not considered since the extinction of the radiative fog aerosol model is superior to the effect of the background climate model. The visibility was altered according to CAT I, CAT II, CAT IIIa and CAT IIIb RVR minima, i.e. 550 m, 350 m, 200 m and 50 m respectively. For each case, the transmission was simulated for three different sensor altitudes, at and nearby the corresponding decision height.

5.1.3 Advective fog

Advective fog was investigated by the same approach as for radiative fog, by simulating the AGT generated atmosphere for winter time, although together with the advective fog aerosol model. The visibility was altered in the same way as for radiative fog, according to CAT I, CAT II, CAT IIIa and CAT IIIb RVR minima. For each case, the transmission was simulated for either two or three different sensor altitudes, at and nearby the corresponding decision height.

5.1.4 Rain

MODRAN offers five different predefined rain models, see Table 5.2.

Table 5.2: MODTRAN defined rain models with description of characteristics.

Rain model	Description
Drizzle	2.0 mm/h at ground and 0.86 mm/h at 1.0 km, stratus cloud.
Light	5.0 mm/h at ground and 2.6 mm/h at 0.66 km, nimbostratus cloud.
Moderate	12.5 mm/h at ground and 6.0 mm/h at 0.66 km, nimbostratus cloud.
Heavy	25.0 mm/h at ground and 0.2 mm/h at 3.0 km, cumulus cloud.
Extreme	75.0 mm/h at ground and 1.0 mm/h at 3.0 km, cumulus cloud.

The rain rates decrease linearly from the ground to the top of the associated cloud model. The maximum rain rate at the ground is however a good approximation for the investigated sensor heights. The cloud models have different properties such as altitude, thickness and water droplet density profiles.

For this simulation transmission was compared for drizzle, light, moderate and heavy rain. Extreme rain was excluded due to its low probability at the chosen location, at lower latitudes such as the tropics, it is however more likely. The four rain intensities were simulated with rural aerosol and default visibility at three sensor altitudes: 15 m, 30 m and 60 m. The sensor zenith angle was constant, 93°.

5.2 Simulation of atmospheric propagation of infrared radiation

In order to accurately simulate the propagation of infrared radiation in the atmosphere, MODTRAN version 6 was used. However, other radiative transfer codes such as LibRadtran were also considered, although after a period of evaluation, it was decided to use MODTRAN instead due to better resolution and a more user-friendly interface. The spectral transmission of the atmosphere for different IR ranges, MWIR and LWIR, enables a quantitative comparison for different atmospheric conditions.

In order to run the simulation, several parameters must be defined. Radiative transfer options, atmospheric profiles, clouds and aerosols, geometry, surfaces and spectral parameters were defined. The atmospheric composition was generated using the AGT as described earlier. Clouds and aerosols, including rain rates, were altered in order to define the investigated weather conditions. The geometry was defined by sensor altitude and sensor zenith angle, simulating a sensor looking down at a target on the ground. The altitude was varied, sensor zenith angle was constantly set to 93° in order to mimic an aircraft approach angle of 3°, see Figure 5.1 for illustration. The radiating ground surface is not of much interest considering the atmospheric transmission, although more important when studying radiance. An urban, lambertian surface was chosen at default temperature (272.2 K for midlatitude winter, see Table 4.3). The spectral parameters were set to include both the visible wavelengths as well as the infrared, i.e. 0.3-14.5 µm.

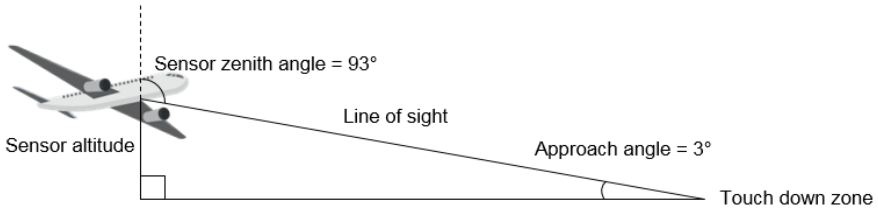

Figure 5.1: Geometrical setup, not to scale. The line of sight is defined by the sensor altitude and sensor zenith angle.

After running a simulation, several output files with different parameters were generated. In this case, the transmittance values were of importance. The transmittance for all wavelengths in the defined range was obtained. Using the programming language Python, the transmittance spectrum was plotted and the average transmittance was calculated. This was done for MWIR, 3-5 µm, and LWIR, 8-14 µm. However, there is attenuation, even in good visibility conditions, around 4.3 µm due to carbon dioxide. This was taken into account when calculating the mean transmittance in the MWIR by simply removing wavelengths in the interval 4.21-4.44 µm from the averaging formula. This is also corrected for by many IR cameras on the market.

5.3 Sensor specifications

For the purpose of this investigation, the contrast between surfaces of different temperatures are of interest and for that reason NETD is an interesting property to consider. Table 5.3 states typical

NETD values for FLIR cameras operating in the two IR intervals of interest, MWIR and LWIR. These values are based on observations made when researching specifications of different FLIR cameras available on the market today. The specifications and assumptions made for the cameras are for two hypothetical cameras based on observed realistic values.

Table 5.3: NETD values for cameras operating in the different wavelength intervals; MWIR and LWIR.

Wavelength band [µm]	NETD [mK]
MWIR: 3-5	18
LWIR: 8-14	20

Worth noting is the fact that the NETD value often is defined for a specific background temperature, for example 20 °C, and may not be entirely accurate if the background temperature differ too much. To be certain of the impact background temperature has on the camera of interest, measurements have to be made. However, in this analysis, NETD is assumed to be constant.

5.4 Calculations

In order to compare the transmittance in various atmospheric conditions, and also put it into perspective to the sensitivity of the cameras, the average transmittance was calculated as described in Section 5.2. The response of the sensors was assumed to be constant for all wavelengths in their respective operational bands. To determine if the transmittance of IR radiation is sufficient for a sensor to detect, the temperature difference at the target and the sensor defined NETD must also be considered. In this case the considered temperature differences at the ground surface are ΔT_{target} = 1 K, 2 K, 5 K, 10 K, 15 K.

Since NETD is the minimum temperature difference the camera can detect, the temperature difference perceived by the sensor, ΔT_{sensor}, must be equal to, or greater than its NETD value. ΔT_{sensor} is the result of the initial temperature difference at the target, ΔT_{target}, in this case for example the difference in temperature between the runway and its surroundings, multiplied by the atmospheric transmittance, τ_{atm}. Since the transmittance was averaged over the investigated IR ranges, MWIR and LWIR, the following equations assumes that all wavelengths are equally transmitted in the range.

$$\Delta T_{sensor} = \tau_{atm} \Delta T_{target} \tag{5.1}$$

The minimum transmittance required is therefore

$$\tau = NETD / \Delta T_{target}. \tag{5.2}$$

For the previously stated NETD values in Table 5.3 and assumed temperature differences at the ground, minimum transmittance are presented in Table 5.4 below.

Table 5.4: Minimum transmittance required for a MWIR sensor with NETD = 18 mK and a LWIR sensor with NETD = 20 mK, in order to interpret temperature differences from 1 to 15 K.

	1 K	2 K	5 K	10 K	15 K
MWIR	$1.8 \cdot 10^{-2}$	$9.0 \cdot 10^{-3}$	$3.6 \cdot 10^{-3}$	$1.8 \cdot 10^{-3}$	$1.2 \cdot 10^{-3}$
LWIR	$2.0 \cdot 10^{-2}$	$1.0 \cdot 10^{-2}$	$4.0 \cdot 10^{-3}$	$2.0 \cdot 10^{-3}$	$1.3 \cdot 10^{-3}$

This is valid under the assumption that the sensor is equally sensitive to all wavelengths in the operating band.

5.4.1 IR detection range

The maximum IR detection ranges in two different types of fog and rain, with different visibility conditions, were determined based on the NETD values of the detectors. $\Delta T = 2K$ was chosen as a realistic temperature difference between the runway and the background, given the conditions at Skavsta Airport with the AGT generated winter atmosphere. This can be observed using the surface temperature model presented in Section 6.3. Important to point out is the fact that ΔT can vary quite a lot depending on location, time of the year and weather conditions. Several simulations were made in order to find the sensor altitudes at which the transmitted temperature difference matched the NETD values. The detection ranges were then calculated using trigonometry given the sensor altitude and the approach angle.

6 Method - Part II: Simulator for infrared imaging

In the following chapter, the different modules of the simulation model are described. Different choices of data and methods used for the simulation model are discussed and motivated. The results from the simulation model will be presented in Chapter 8.

6.1 System architecture

The architecture of the simulation model can be seen in Figure 6.1. Several smaller modules with different inputs were needed in order to properly simulate the situations of interest. The first module was used to classify different materials present in an image since different materials have different properties regarding emittance of infrared radiation. A model to estimate surface temperature was needed since the temperature difference of different surfaces is of importance. The propagation of infrared radiation was simulated using MODTRAN. The transmittance of the temperature difference defined at the ground was calculated based on transmittance spectra generated with MODTRAN. The temperature difference perceived by the sensor, together with the camera response properties NETD and SiTF, were used to generate a grayscale image of a landing approach. The details of the different modules are described in upcoming sections.

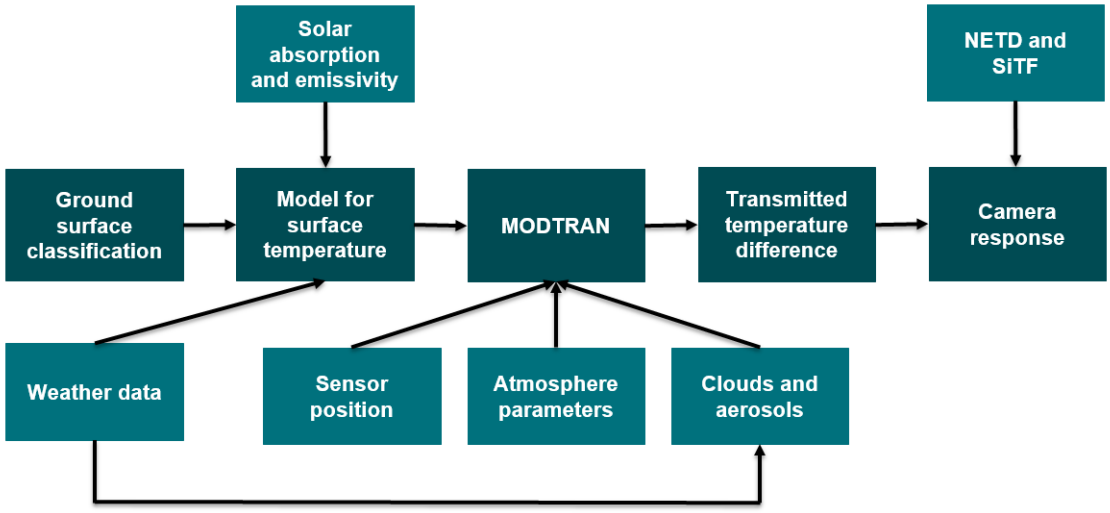

Figure 6.1: Conceptual block-diagram of the simulation model.

6.2 Ground surface classification

Since different materials emit infrared radiation differently, the ground surface classification is an important module of the simulation. Several ways to classify ground have been investigated in this project, however many methods were insufficient or too specific.

Since only satellite images of airports were available, the classification of materials was based on these types of images. The satellite images were collected from Google Earth Pro, since the quality of these images was remarkably better than images that could be retrieved online.

Supervised classification of surface materials was initially performed using QGIS. QGIS is a free and open-source geographic information system (GIS) application that supports viewing, editing, and analysis of geospatial data. Different areas in images were manually classified as specific materials. After manual classification of different areas, new images could be classified. The classification was inadequate in several aspects which is why other methods were considered.

Unsupervised classification was attempted by applying k-means clustering on satellite images in Python. The clustered groups were based on RGB-colors for each pixel and the number of clusters could be defined. However, different surface materials which should ideally have been classified as different materials belonged to the the same classification. Information was thus lost when performing this type of ground classification.

Finally, the classification of ground materials at the relevant airport location was imported from OpenStreetMap. Different classifications of ground was imported as polygon areas describing the border coordinates of different ground surfaces. The different ground surfaces that were considered: asphalt, grass, forest, water and concrete surface of buildings. Every polygon area was assigned with a color based on the surface it represented. The classified areas were plotted onto a satellite image to ensure that the classified areas matched the actual surface areas seen on the satellite image.

Considering the objectives and satellite data used, only a confined number of classes were needed. The data available for the surface temperature model was limited regarding emissivity for different materials. Therefore a better classification of the ground surfaces would have been of limited use in this case.

6.3 Model for surface temperature

Unlike air temperature, the temperature of the ground surface is rarely measured directly and is not available on a large scale online. In order to estimate the ground surface temperature, different options were considered. An alternative was to utilize data from satellites such as Landsat or ASTER in order to derive the surface temperature, although the resolution was found to be insufficient for the purpose of this study. A simplified physics model for estimation of surface temperature was thus applied, considering heat fluxes by radiation, convection and conduction.

The estimation of the surface temperature considered the emissivity of the surfaces defined in the classification, along with several other factors, such as solar irradiation, air temperature and wind speed, etc. The model described in Section 2.2.2 takes into account the absorbed solar radiation, the emitted thermal radiation as well as the heat exchange by convection and conduction. Equation 2.17 in Section 2.2.2 was rewritten as

$$\epsilon\sigma_e {T_s}^4 + (h_c + \frac{\kappa}{\Delta x})T_s - \alpha E_{in} - h_c T_{amb} - \frac{\kappa}{\Delta x} T_{layer} = 0 \tag{6.1}$$

with the simplification $\alpha = \epsilon$ as discussed in Section 2.2.1. The fourth-degree polynomial was then solved numerically for the surface temperature T_s using Python. Solar irradiation, air temperature and wind speed were taken from SMHI for the day and time in question and ϵ and κ are presented in Tables 4.1 and 4.2 in Section 4.2. The temperature T_{layer} was calculated by using the model developed by Plauborg [59]. The model estimates the temperature at 10 cm depth in soil and has therefore been used on grass and soil surfaces, but also on asphalt surfaces since the thermal conductivity is similar to soil.

The estimation of surface temperature was however simplified for surfaces covered by snow, since the thermal conductivity for snow is very small and the contribution of conductive heat transfer was therefore neglected. The conduction term was also excluded for forest since trees are airy and doesn't conduct heat in the same sense as for example asphalt and soil.

6.3.1 Validation of surface temperature model

In order to validate the surface temperature model, the temperature-based method briefly mentioned in Section 1.4.1 was chosen, since the resolution provided by the radiance-based and cross-validation method is not sufficient for this purpose, with heterogeneous surfaces.

Validation of the surface temperature model was performed by comparing the simulation values with measured temperature values from a thermal camera, *Fluke Ti10*, see Figure 6.2 below. According to the documentation, the accuracy of the camera is $\pm$ 2°C. The temperature of different surfaces was measured with the thermal camera at different weather conditions and the same conditions were then simulated by extracting weather parameters from SMHI. The measurements were carried out outside of Saab's office in Järfälla.

Figure 6.2: Fluke Ti10, the thermal camera used for validation of the surface temperature model [60].

Measurements were taken of available surfaces, i.e. grass, asphalt, soil and on certain days also snow. For every surface type, five measurements were made and the mean value was calculated in attempt to reduce random errors. Every measurement day was categorized as either sunny, cloudy, rainy or snowy. This was done in order to see if the temperature model performed differently in different weather conditions. The root-mean-square error (RMSE) of the model performance compared to the measured mean temperatures was calculated as well as the mean absolute error (MAE) in degrees Celsius.

The temperature model did not perform as desired, since the temperatures were constantly underestimated in comparison to the temperatures measured with the thermal camera. Correction factors were therefore added to the temperature model.

The correction factors were based on previous simulations compared to the measured temperatures. The mean error was determined for every surface type in every weather category. This value was then added to the surface temperature model and depended on the surface and classification of weather condition.

New simulations and temperature measurements were made in order to validate the temperature model together with the correction factors. Again, the RMSE of the model performance compared to the measured mean temperatures was calculated as well as the MAE in degrees Celsius.

6.4 MODTRAN simulations

The atmospheric transmission of IR was simulated with MODTRAN. To provide the reader with an understanding of how the simulation model works, one weather scenario has been chosen for the simulation. However, changing the settings in MODTRAN could generate other desired weather conditions.

In this simulation, an environment with radiative fog has been chosen. The surface meterological range, or visibility, was set according to CAT II RVR minimum, i.e. 350 m. The background atmosphere was generated by the AGT for the position of Skavsta Airport in the beginning of January. The sensor position was set according to CAT II decision height and standard approach angle 3°, i.e. sensor altitude 30 m and zenith angle 93°. The transmission was simulated for wavelengths in the interval 0.3-14.5 µm, and thus both MWIR and LWIR was covered.

6.5 Image construction

The temperatures of the surfaces in the classified satellite image were determined by the surface temperature model (6.1). The surface temperatures were modeled with parameters corresponding to a foggy day in January.

The most commonly occurring surface temperature in the image, in this case the grass temperature, was set as background. The differences between temperatures of the other surfaces and the background was ΔT_{target}.

Since the field of view of the camera covers the whole runway, viewing angle and thereby the slant path varies to different parts of the scene. This means that the transmittance will be lower for objects and surfaces further away from the camera. This has been accounted for when constructing the image by calculating the slant path distance to different pixels in the image and changing the transmittance according to the CAT II curve in Figure 7.5. The temperature difference perceived by the sensor after atmospheric propagation, ΔT_{sensor}, was calculated with Equation 5.1.

When ΔT_{sensor} had been calculated for all pixels, grayscale values were assigned. This was done by using the SiTF, see Section 3.3.1. In this case, the SiTF was assumed to be linear over the interval $-2 < \Delta T_{sensor} < +2$, see Image 6.3 below. The reference temperature of grass was assumed to be at $\Delta T_{sensor} = 0$, which corresponds to 50 % of 256, a grayscale value of 128.

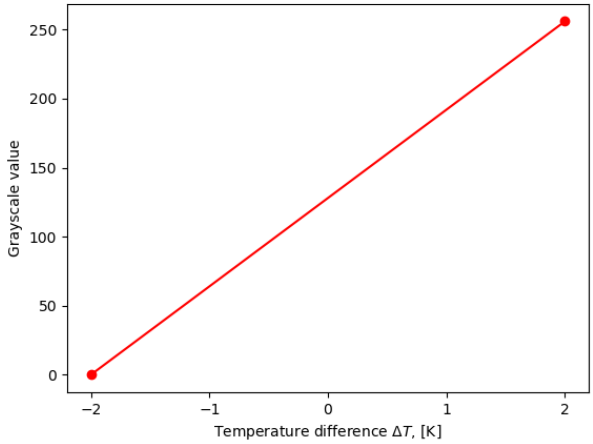

Figure 6.3: Linear approximation of SiTF.

The grayscale values generated based on the SiTF were assigned to the different pixels. Since the visibility in the MODTRAN simulation was defined according to CAT II, the image generated of the runway is seen from an approximate height of 30 m which corresponds to a slant path of 573 m to the start of the runway. The image was generated based on the classified image but the perspective was changed in order to get the view of a camera at a height of 30 m.

In order to make the image more realistic, noise was added to the image. The noise was assumed to have a normal distribution and the standard deviation of the noise, σ, was calculated using Equation 3.1. A grayscale noise level generated with the function np.random.normal in Python, was added to all pixels in the image.

The constructed image was compared to a real IR image. The image was taken by a LWIR camera and shows a corresponding landing approach to Skavsta airport during good weather conditions, i.e. no rain or fog.

7 Results - Part I: Infrared transmittance in different weather conditions

The results of the infrared transmittance analysis described in Chapter 5 are presented in this chapter. The results are divided based on different weather conditions and visibilities defined by the different ILS categories.

7.1 MODTRAN simulations

7.1.1 Clear weather

Transmission was simulated for clear weather, i.e. no clouds, fog or rain. Two different sensor positions were chosen and the transmittance of IR for the both cases were compared in order to see to what extent distance decrease the radiation. The transmittance spectra are shown below, see Figure 7.1.

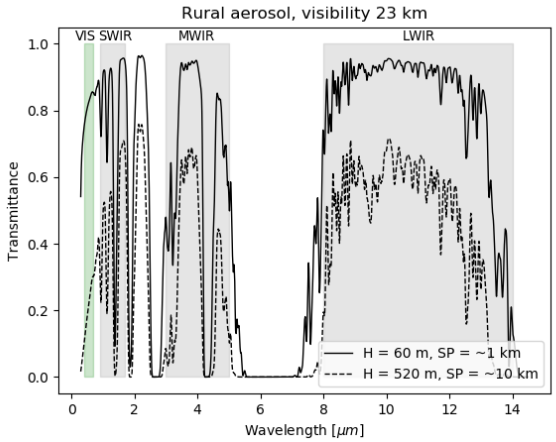

Figure 7.1: Spectral transmission at two different heights (H) in clear weather conditions. Slant path (SP) is the distance from the sensor to the ground with a 3°angle relative to the horizontal ground. The aersol model used was defined by rural aerosols with a visibility of 23 km.

The average transmittance in MWIR and LWIR was calculated for both altitudes and the results are presented in Table 7.1.

Table 7.1: Averaged transmittance in the MWIR and LWIR bands for clear weather conditions at 60 m and 520 m altitude.

	60 m	520 m
MWIR	0.7245	0.3507
LWIR	0.8214	0.4627

As can be seen in Figure 7.1 and Table 7.1, the transmittance is decreasing as the altitude and slant path increases. Although, when comparing the transmittance with the minimum transmittance required by the defined sensors, see Table 5.4 in Section 5.3, it's clearly enough in all four cases considering wavelength interval and sensor altitude. The limiting factor when the sensor altitude and slant path are increased is therefore not the transmittance or NETD, but more likely the spatial resolution of the camera.

Based on the transmittance in the two intervals respectively, the temperature differences at the sensor after propagating through the atmosphere can be calculated by Equation 5.1.

The minimum temperature differences detectable by the defined sensors were also calculated based on the given atmosphere and transmittance by rearranging Equation 5.2, see Table 7.2.

Table 7.2: Minimum temperature differences in Kelvins, detectable by the given sensors for different sensor altitudes.

	60 m	520 m
MWIR	0.025	0.051
LWIR	0.024	0.043

The atmospheric transmittance was compared for summer and winter time. The sensor position was defined by the altitude, 60 m, and 93° sensor zenith. See Figure 7.2 for transmittance spectrum.

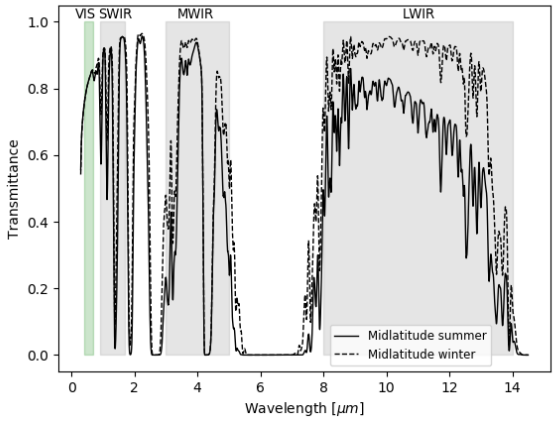

Figure 7.2: Comparison of transmission between summer and winter time in clear weather conditions. The aersol model used was defined by rural aerosols with a visibility of 23 km. Sensor altitude 60 m with zenith angle 93° defined the line of sight.

The transmittance does not differ much for the short wavelengths, below MWIR. There is a slight difference in the MWIR band, and a substantial difference for wavelengths in the LWIR band with highest transmittance in winter time. The difference in the atmospheric modeling of summer and winter is primarily the increased absolute humidity during summer time, which implicates higher extinction and a slightly shifted size distribution. Even though the relative humidity is actually higher during winter, the temperature is higher during summer and the air can therefore hold more water vapor.

Several aerosol models were also compared in terms of transmittance. Rural, urban and maritime aerosols were simulated with their corresponding default visibilities at a sensor altitude of 520 m. The transmittance spectra are presented below, see Figure 7.3.

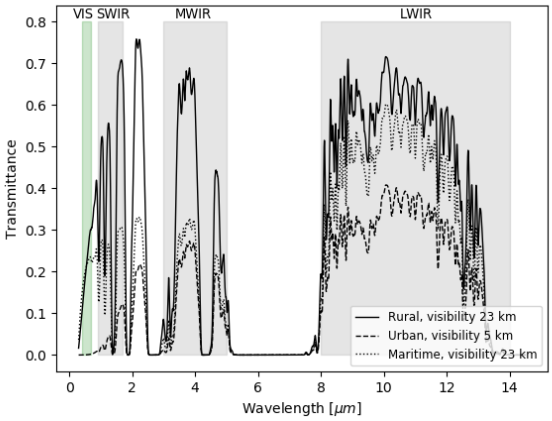

Figure 7.3: The figure shows a comparison of spectral transmission for different aerosol models in clear weather conditions. The sensor position is at 520 m altitude with a zenith angle of 93° and a slant path of approximately 10 km.

Rural aerosol exhibit a higher transmittance throughout the investigated wavelengths, than maritime and urban aerosol. The difference is especially noticeable for wavelengths shorter than 5 µm. The urban aerosols have the lowest transmittance. The composition and size distribution of aerosols determine the extinction factor and therefore also the transmittance. Urban aerosol are assumed to have the same size distribution as the rural aerosol, the difference lies in the refractive index due to the addition of combustion and industrial particles. The default visibility range is much shorter for the urban model due to higher concentrations of aerosols and thereby the greater attenuation.

7.1.2 Radiative fog

Transmission was simulated with radiative fog and different visibility conditions, according to CAT I, CAT II, CAT IIIa and CAT IIIb. The plotted results can be seen in Figure 7.4.

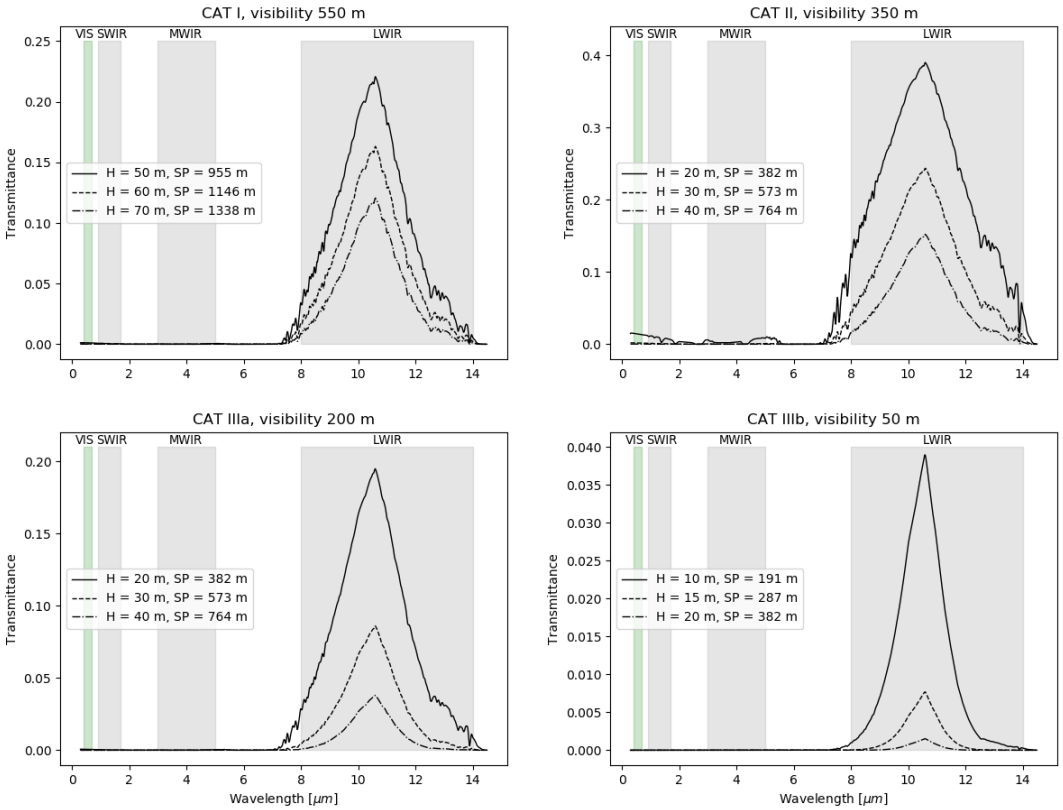

Figure 7.4: Spectral transmission in low visibility conditions according to CAT I, CAT II, CAT IIIa and CAT IIIb, at three different heights (H), at decision height, one below and one above decision height. Slant path (SP) is the distance from the sensor to the ground with a 3° angle relative to the horizontal ground. The radiative fog aerosol model was used.

The four plots in Figure 7.4 shows the transmittance per wavelength in CAT I, CAT II, CAT IIIa and CAT IIIb visibility at three different heights. As can be seen in the spectra, the transmittance in the SWIR and MWIR bands are exceedingly small and almost all radiation shorter than 8 microns seem to be attenuated by the atmosphere. In Table 7.3 below, the averaged transmittance are presented for both MWIR and LWIR.

Table 7.3: Averaged transmittance in the MWIR and LWIR bands for different visibility conditions at decision height.

	CAT I	CAT II	CAT IIIa	CAT IIIb
MWIR	$3.533 \cdot 10^{-5}$	$3.087 \cdot 10^{-4}$	$1.251 \cdot 10^{-6}$	$6.053 \cdot 10^{-12}$
LWIR	$6.881 \cdot 10^{-2}$	$1.187 \cdot 10^{-1}$	$3.046 \cdot 10^{-2}$	$1.713 \cdot 10^{-3}$

The calculated average transmittance together with the NETD limitations gives the minimum temperature differences detectable by the defined sensors (Equation 5.2), see Table 7.4.

Table 7.4: Minimum temperature differences in Kelvins, detectable by the given sensors for different visibility conditions at decision height.

	CAT I	CAT II	CAT IIIa	CAT IIIb
MWIR	510	58	14000	$2.9 \cdot 10^9$
LWIR	0.29	0.17	0.66	12

The values in Table 7.4 show that a temperature difference of less than 1 K at the ground can be interpreted by the defined LWIR sensor at decision height in both CAT I, CAT II and CAT IIIa visibility for the given atmosphere. In CAT IIIb visibility, a higher temperature difference is required by a sensor with NETD = 20 mK in order to be seen at 15 m height, or by proceeding further down to 10 m height, a temperature difference of 2 K can be observed. The results also show that the transmittance in MWIR is not sufficient in any of the visibility ranges investigated.

The transmittance of MWIR and LWIR in radiative fog as a function of slant path can be seen in Figure 7.5 for different visibility conditions. As a reference, the green lines in the plots correspond to the minimum transmittance an IR camera with NETD value 18 mK or 20 mK respectively, require in order to detect a temperature difference of 2 K according to Table 5.4.

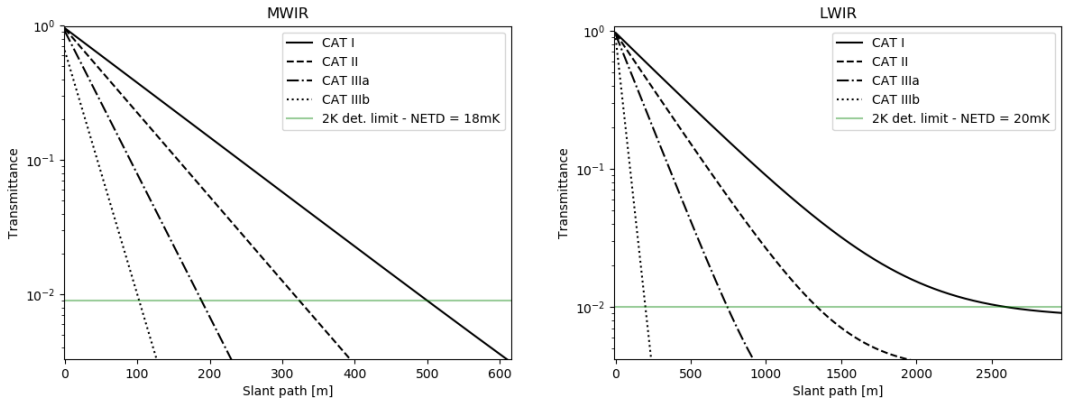

Figure 7.5: Transmittance as a function of slant path for different visibilities. The green lines correspond to the 2 K detection limit for a MWIR camera with NETD = 18 mK and a LWIR camera with NETD = 20 mK.

Based on the relationship between transmittance and slant path, the maximum IR detection range was determined for different visibility conditions for a temperature difference, target to background, of 2 K, considering the NETD thresholds. The results can be seen in Table 7.5.

Table 7.5: Maximum detection range in MWIR and LWIR respectively for different visibility conditions in radiative fog. The range considers NETD values 18 mK and 20 mK for MWIR and LWIR cameras respectively.

CAT	Visibility	IR detection range [m]	
	VIS	MWIR	LWIR
I	550	500	2100
II	350	330	1300
IIIa	200	170	780
IIIb	50	38	190

Considering the results above for the given weather scenario with radiative fog, an LWIR camera is very beneficial compared to a MWIR camera or no IR camera at all. The transmittance is superior in LWIR which reflects in the detection range. The IR detection range in LWIR is almost 4 times the visual range in all the investigated visibility conditions. The detection range in MWIR is even shorter than the visual range.

7.1.3 Advective fog

Transmission was simulated in advective fog and different visibility ranges, according to CAT I, CAT II, CAT IIIa and CAT IIIb. The plotted results can be seen in Figure 7.6.

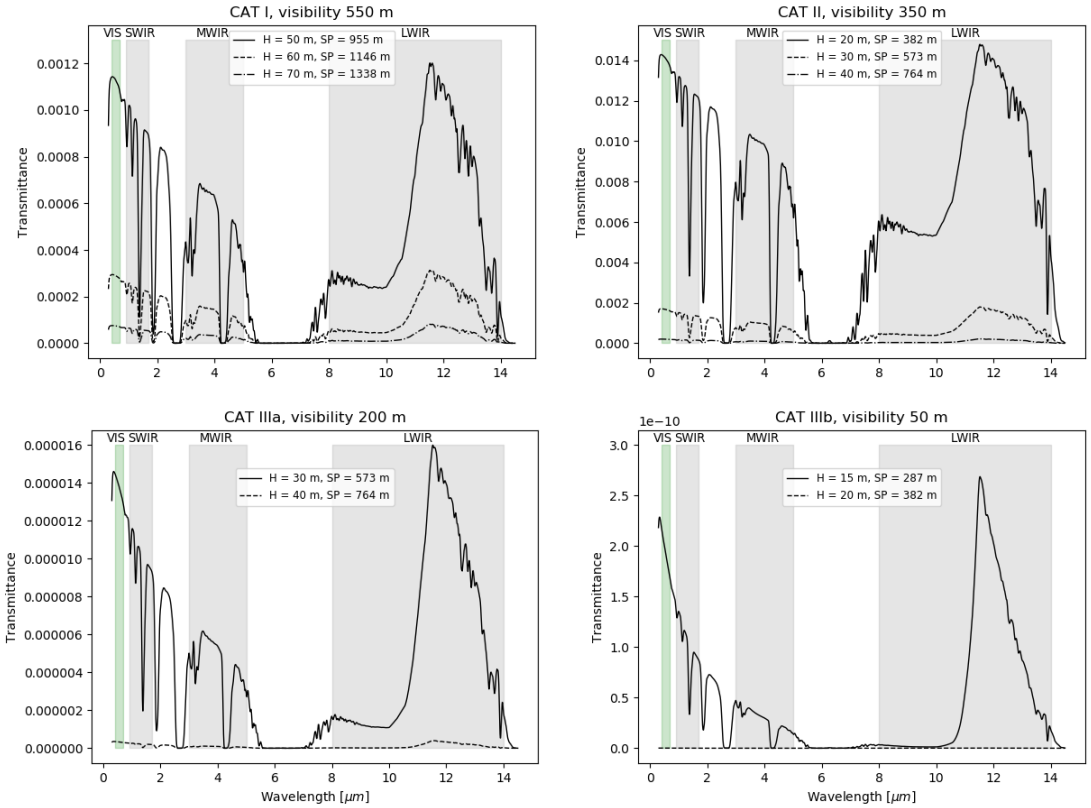

Figure 7.6: Spectral transmittance in low visibility conditions according to CAT I, CAT II, CAT IIIa and CAT IIIb, at two or three different heights (H). Slant path (SP) is the distance from the sensor to the ground with a 3° angle relative to the horizontal ground. The advective fog aerosol model was used.

The four plots in Figure 7.6 show the transmittance per wavelength in CAT I, CAT II, CAT IIIa and CAT IIIb visibility at different sensor altitudes. The spectra show a more even transmittance in all three IR bands, and also in the visible band, compared to the case with radiative fog. However, the transmittance in the LWIR band is substantially lower than for radiative fog. In Table 7.6 below, the averaged transmittance are presented for both MWIR and LWIR.

Table 7.6: Averaged transmittance in the MWIR and LWIR bands for different visibility conditions at decision height.

	CAT I	CAT II	CAT IIIa	CAT IIIb
MWIR	$1.135 \cdot 10^{-4}$	$8.217 \cdot 10^{-4}$	$4.656 \cdot 10^{-6}$	$2.939 \cdot 10^{-11}$
LWIR	$1.282 \cdot 10^{-4}$	$8.701 \cdot 10^{-4}$	$5.718 \cdot 10^{-6}$	$6.499 \cdot 10^{-11}$

The minimum temperature differences detectable by the sensors are presented in Table 7.7. Those values are calculated by Equation 5.2, from the average transmittance together with the NETD limitations.

Table 7.7: Minimum temperature differences in Kelvins, detectable by the given sensors for different visibility conditions at decision height.

	CAT I	CAT II	CAT IIIa	CAT IIIb
MWIR	160	22	4000	$6.1 \cdot 10^8$
LWIR	160	23	3500	$3.1 \cdot 10^8$

The results show that the transmittance in both MWIR and LWIR is insufficient in all of the visibility ranges investigated. The minimum temperature differences necessary, especially for CAT IIIa and CAT IIIb, are not at all realistic in the situation of an aircraft approach and landing. A temperature difference around 20 K or 160 K is very unlikely to be found in the sense of runway contrast, although aircraft or other blocking vehicles may have hot engines or other hot spots which could perhaps be detected.

The transmittance of MWIR and LWIR in advective fog as a function of slant path can be seen in Figure 7.7 for different visibility conditions. The green lines in the plots correspond to the minimum transmittance an IR camera with NETD value 18 mK or 20 mK respectively, require in order to detect a temperature difference of 2 K according to Table 5.4.

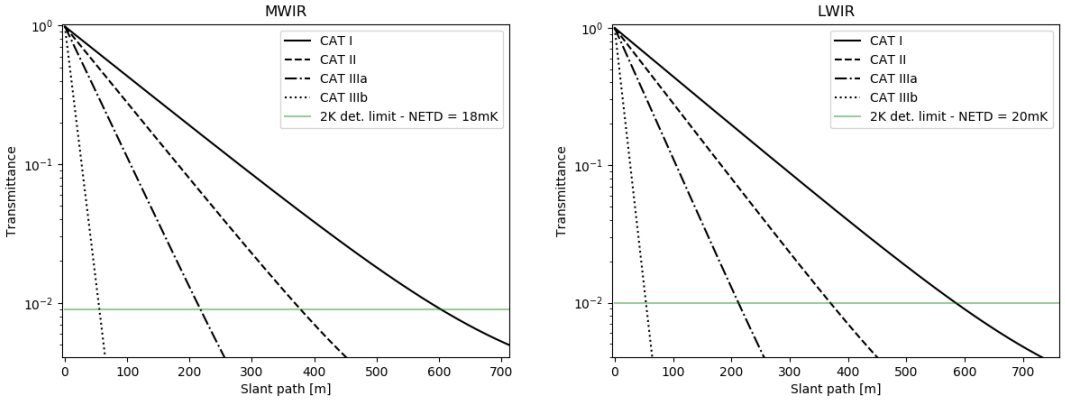

Figure 7.7: Transmittance as a function of slant path for different visibilities. The green lines correspond to the 2 K detection limit for a MWIR camera with NETD = 18 mK and a LWIR camera with NETD = 20 mK.

The maximum IR detection range was determined for different visibility conditions for a temperature difference, target to background, of 2 K, considering the NETD thresholds. The results can be seen in Table 7.8.

Table 7.8: Maximum detection range in MWIR and LWIR respectively for different visibility conditions.

CAT	Visibility	IR detection range [m]	
	VIS	MWIR	LWIR
I	550	590	580
II	350	380	370
IIIa	200	220	210
IIIb	50	55	54

For advective fog, the visibility and IR detection range is equally low. The pilot would not benefit from an IR camera, neither MWIR nor LWIR, in this particular case of advective fog. As can be observed in the plots in Figure 7.6, the transmittance is relatively even in the entire spectrum, which is why the visibility and the IR detection range is very similar.

7.1.4 Rain

Transmittance was simulated for different rain intensities at three different sensor altitudes. The spectra can be seen in Figure 7.8 below.

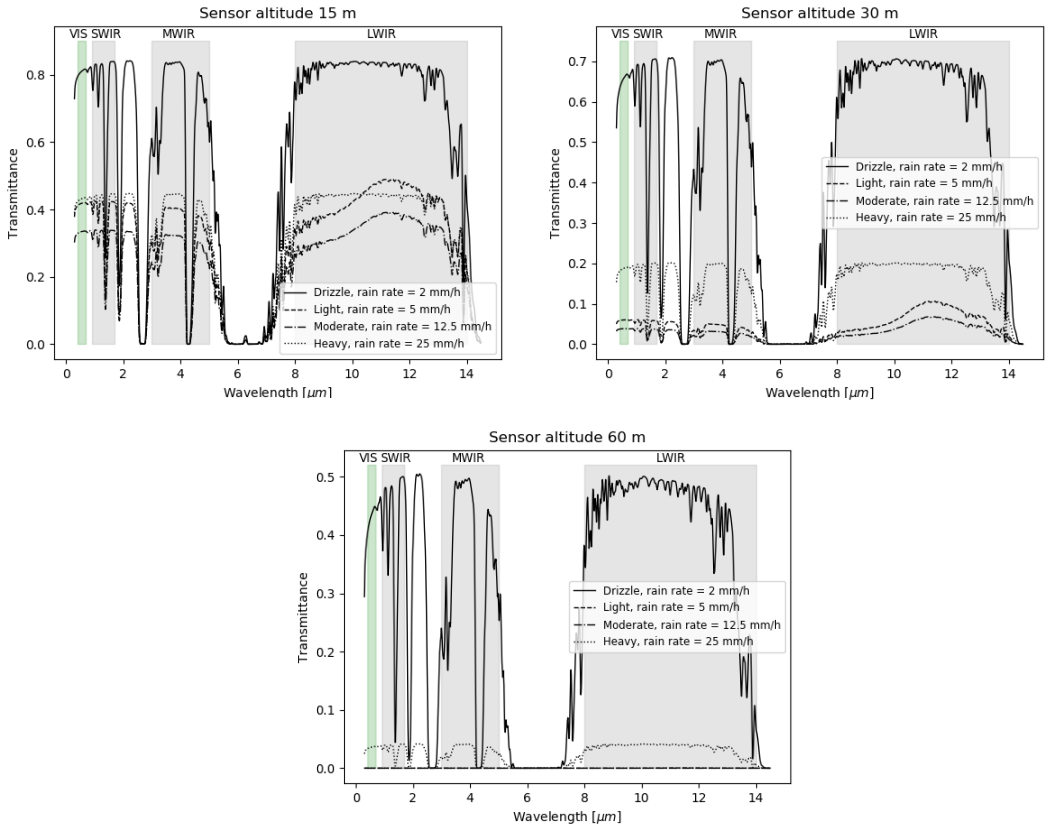

Figure 7.8: Spectral transmission for different sensor altitudes and rain rates. Rural aerosol with default visibility was used for the atmospheric model.

As can be seen in the transmittance spectra at 30 and 60 m altitude in Figure 7.8, light and moderate rain tend to attenuate much more radiation than heavy rain. In this simulation with MODTRAN, the reason is that different cloud models are used when simulating different rain intensities. Drizzle is modeled with a stratus cloud, light and moderate rain are modeled with a nimbostratus cloud, and heavy rain is modeled with a cumulus cloud. Different clouds have different properties, e.g. altitude and thickness. The nimbostratus cloud is the only cloud model with a positive cloud density below 160 m altitude. The nimbostratus cloud has a water droplet density that increases linearly from 0.0 g/m^3 at 0.0 m to 0.3 g/m^3 at 160 m. In those cases, the attenuation is a combination of cloud and rain attenuation. For clarifying purpose the transmission spectra for light and moderate rain are presented alone in order to better visualize their amplitudes, see Figure 7.9.

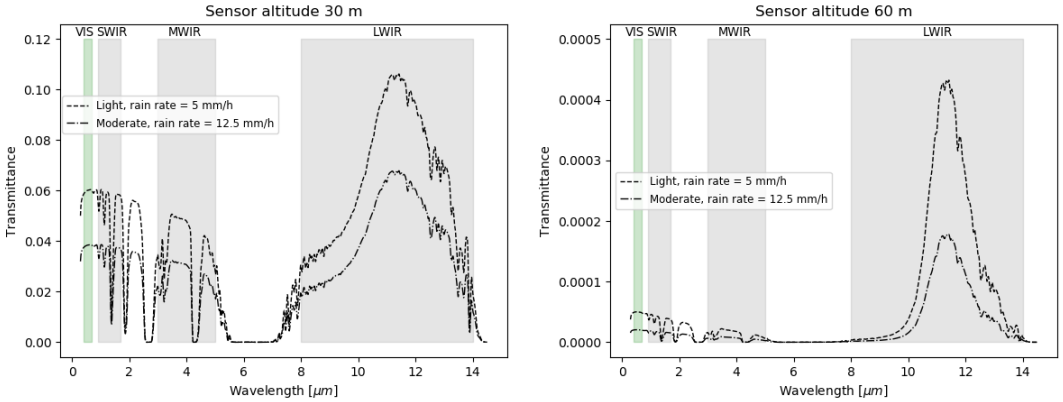

Figure 7.9: Clarifying illustration of light and moderate rain at sensor altitude 30 and 60 m.

The average transmittance calculated in MWIR and LWIR are presented in Table 7.9 and 7.10 for 30 m and 60 m respectively.

Table 7.9: Averaged transmittance in the MWIR and LWIR bands for different rain models at 30 m altitude.

	Drizzle	Light	Moderate	Heavy
MWIR	0.5784	$3.996 \cdot 10^{-2}$	$2.554 \cdot 10^{-2}$	0.1646
LWIR	0.6356	$6.363 \cdot 10^{-2}$	$4.068 \cdot 10^{-2}$	0.1811

Table 7.10: Averaged transmittance in the MWIR and LWIR bands for different rain models at 60 m altitude.

	Drizzle	Light	Moderate	Heavy
MWIR	0.3761	$1.435 \cdot 10^{-5}$	$5.897 \cdot 10^{-6}$	$3.113 \cdot 10^{-2}$
LWIR	0.4275	$1.260 \cdot 10^{-4}$	$1.176 \cdot 10^{-5}$	$3.545 \cdot 10^{-2}$

As can be seen in Table 7.9, the transmittance is sufficient in all the investigated rain intensities for detection in both MWIR and LWIR at 30 m altitude. That is, the transmittance is greater than the sensor limitations stated in Table 5.4. However this is not the case when the sensor altitude is increased to 60 m. Table 7.10 show a significant decrease in transmission in light and moderate rain.

The minimum target temperature differences detectable by the sensors are presented in Table 7.11, based on the average transmittance and the minimum transmittance required by the sensors defined in Table 5.4.

Table 7.11: Minimum temperature differences in Kelvins, detectable by the given sensors for different rain conditions at 60 m altitude.

	Drizzle	Light	Moderate	Heavy
MWIR	$4.8 \cdot 10^{-2}$	1300	3100	0.58
LWIR	$4.7 \cdot 10^{-2}$	160	1700	0.56

From the results in Table 7.11, only the transmittance through drizzle and heavy rain are sufficient in order to detect temperature differences reasonable for this purpose. Let's keep in mind however, the contributing cloud attenuation, in the case of higher clouds the transmittance is significantly increased. Light and moderate rain was therefore also simulated with cumulus clouds, in order to eliminate the cloud contributing attenuation, the spectra can be seen in Figure 7.10. The average transmittance in LWIR is then 0.2549 and 0.1034 at 60 m for light and moderate rain respectively, which is enough for detection.

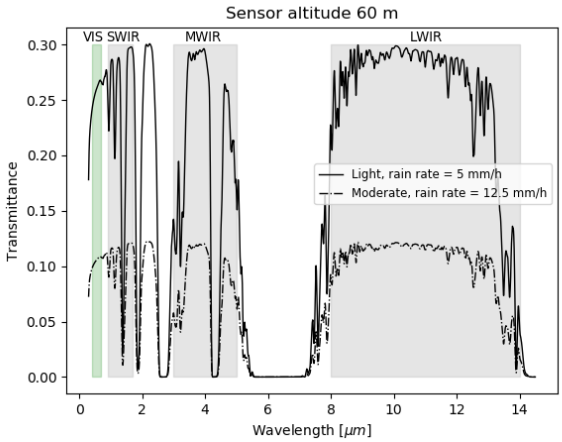

Figure 7.10: Spectral transmittance for light and moderate rain, modeled with cumulus clouds.

The transmittance of MWIR and LWIR in rain as a function of slant path can be seen in Figure 7.11. As a reference, the green lines in the plots correspond to the minimum transmittance an IR camera with NETD value 18 mK or 20 mK respectively, require in order to detect a temperature difference of 2 K according to Table 5.4.

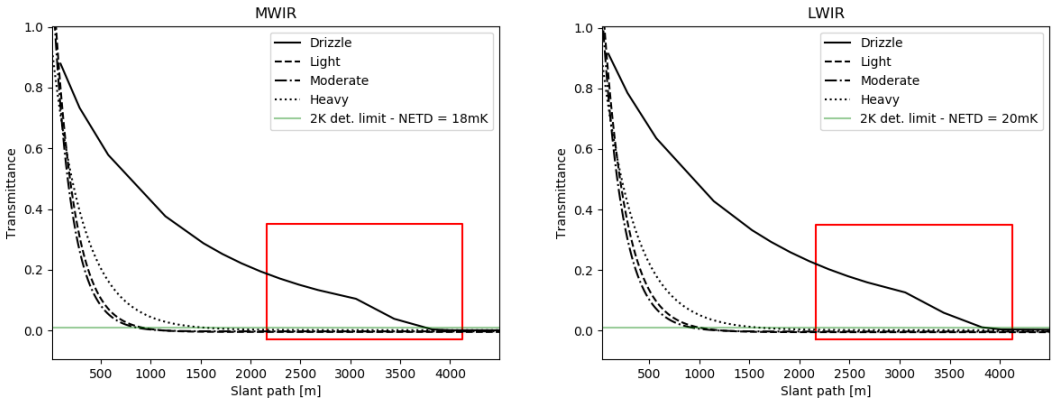

Figure 7.11: Transmittance as a function of slant path for different visibilities. The green lines correspond to the 2 K detection limit for a MWIR camera with NETD = 18 mK and a LWIR camera with NETD = 20 mK.

The appearance of the drizzle curve in Figure 7.11, marked by the red box, is explained by the stratus cloud model in MODTRAN. The stratus cloud has a water droplet density that increases linearly from 0.0 g/m^3 at 160 m to 0.150 g/m^3 at 330 m and so on. Therefore at 160 m altitude, corresponding to a slant path of 3076 m, attenuation by the stratus cloud is added to the rain attenuation.

The maximum IR detection range was determined for different rain intensities for a temperature difference, target to background, of 2 K, considering the NETD thresholds. The results can be seen in Table 7.12. Since the visibility is not defined in the simulation, a comparison between the visibility and IR detection range was not possible.

Table 7.12: Maximum detection range in MWIR and LWIR respectively for different rain intensities.

Rain type	IR detection range [m]	
	MWIR	LWIR
Drizzle	3800	3800
Light	740	790
Moderate	710	740
Heavy	1600	1600

The attenuation increases with the rain intensity, i.e. the rain rate, although there is no spectral dependence in the investigated wavelength interval. Theoretically, the reason is the fact that raindrops in general are much larger than the wavelengths in question and thereby the size parameter is a large value. As can be seen in Figure 2.2, the extinction efficiency asymptotically approaches a value of approximately two, as the size parameter increases, which means that for a distribution of rain drop sizes, the scattering does not vary much with wavelength in the visible and infrared.

7.1.5 Comparison of clear weather and fog

In order to better see the difference in attenuation between radiative and advective fog, and also in the absence of clouds, fog and rain, the transmittance spectra was plotted together in Figure 7.12.

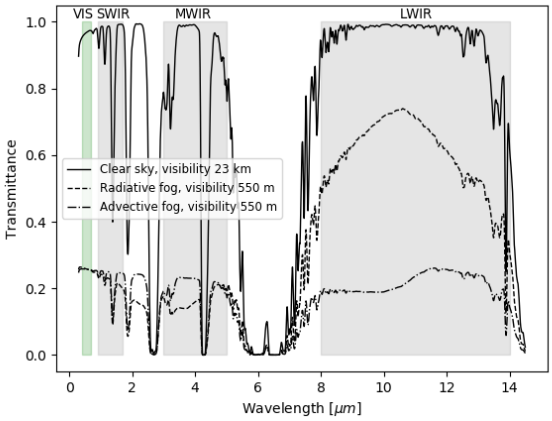

Figure 7.12: Comparison of transmittance in clear weather condition, radiative fog and advective fog. Sensor position at 10 m height with slant path range 191 m.

As discussed earlier, the attenuation differs considerably between radiative and advective fog. The greatest difference is observed in LWIR with more attenuation in advective fog, in MWIR however, the attenuation is greater in radiative fog. In the clear weather scenario, the transmittance is very high in the atmospheric window, as expected.

8 Results - Part II: Simulator for infrared imaging

The results from the ground surface classification, the surface temperature model validation, the atmospheric propagation simulation of infrared radiation as well as the image construction are described in Chapter 6 are presented in this chapter.

8.1 Ground surface classification

The result of the ground surface classification using data from OpenStreetMap can be seen in Figure 8.1. Different colors correspond to different classifications defined in the OpenStreetMap API. The coordinates of different areas are ploted on a satellite image in order to confirm that the classification is correct.

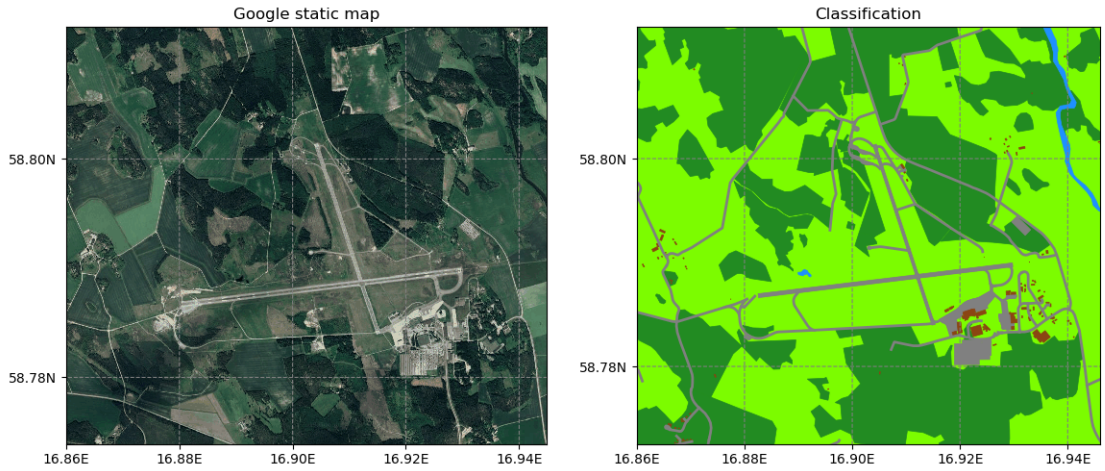

Figure 8.1: Ground surface classification based on OpenStreetMap data.

8.2 Surface temperature model

The measurements of surface temperature of different materials were performed during February to April in varied weather conditions and at different times of the day. The results from the measurements compared to the surface temperature model have been summarized in different categories, i.e. weather conditions. The measurements days have been categorized to sunny, cloudy, rainy or snowy days. This was done in order to see how the model performed in different weather conditions. The air temperature varied for different measurement days. The RMSE and

MAE values in the tables below correspond to the performance of the surface temperature model with the added correction factors as described in Section 6.3.1.

The average RMSE and the average MAE for different surfaces of measurements taken on days categorized as sunny can be seen in Table 8.1 below.

Table 8.1: Results of comparison between measured surface temperature and simulation model for sunny days.

Surface	$\overline{\text{RMSE}}$ [°C]	$\overline{\text{MAE}}$ [°C]
Grass	2.09	1.90
Asphalt	1.93	1.77
Soil	1.97	1.78

The average RMSE and the average MAE for different surfaces of measurements taken on days categorized as cloudy can be seen in Table 8.2 below.

Table 8.2: Results of comparison between measured surface temperature and simulation model for cloudy days.

Surface	$\overline{\text{RMSE}}$ [°C]	$\overline{\text{MAE}}$ [°C]
Grass	1.98	1.90
Asphalt	1.59	1.55
Soil	1.86	1.73

The average RMSE and the average MAE for different surfaces of measurements taken on days categorized as rainy can be seen in Table 8.3 below.

Table 8.3: Results of comparison between measured surface temperature and simulation model for rainy days.

Surface	$\overline{\text{RMSE}}$ [°C]	$\overline{\text{MAE}}$ [°C]
Grass	1.03	0.91
Asphalt	1.06	0.96
Soil	2.58	2.39

The average RMSE and the average MAE for different surfaces of measurements made on days categorized as snowy can be seen in Table 8.4 below. During snowy days, snow and asphalt were the only available surfaces for measurements.

Table 8.4: Results of comparison between measured surface temperature and simulation model for snowy days.

Surface	$\overline{\text{RMSE}}$ [°C]	$\overline{\text{MAE}}$ [°C]
Asphalt	1.96	1.86
Snow	0.83	0.76

8.3 Simulation and image construction

The temperatures for different surfaces simulated by the temperature model can be seen in Table 8.5 below. The temperatures are simulated based on weather parameters from a foggy day in January. Since the temperature model couldn't be validated for all surfaces, i.e. buildings and forest, and thus no correction factor could be added, an approximated temperature has been assigned to these surfaces.

Table 8.5: Simulated ground surface temperatures.

Surface	Simulated temp. [°C]
Grass	-1.2
Asphalt	-0.30
Soil	-2.4
Forest	1.0
Buildings	2.0

The background temperature was defined based on the surface that was most common in the image, in this case grass. Since the background temperature was defined as -1.2 °C, the temperature differences for each surface to the background can be seen in Table 8.6 below. The chosen weather scenario and visibility defined according to CAT II, gives an average transmittance in the LWIR interval according to Table 7.3. The temperature difference at the ground surface, ΔT_{target}, multiplied by the average transmittance gives the temperature difference transmitted to the sensor, ΔT_{sensor}, seen in Table 8.6 below. The ΔT_{sensor} values perceived by the camera are valid for a slant path of 537 m, i.e. the start of the runway.

Table 8.6: Temperature difference against the background for different surfaces.

Surface	ΔT_{target} [°C]	ΔT_{sensor} [°C]
Grass	0	0
Asphalt	0.90	0.12
Soil	1.2	0.14
Forest	2.2	0.26
Buildings	3.2	0.38

The temperature differences transmitted from the start of the runway are resolvable given the NETD value 20 mK. As described in Section 6.5, the transmittance will be lower as the slant path is increased. This was accounted for when assigning grayscale values to the pixels in the image.

The resulting image of a landing approach at a height of 30 m with a slant path of 573 m can be seen in Image 8.3 below. The most important contrast is between the grass and the runway. These surfaces are considered by the temperature model and as can be seen in Figure 8.3, they are distinguishable.

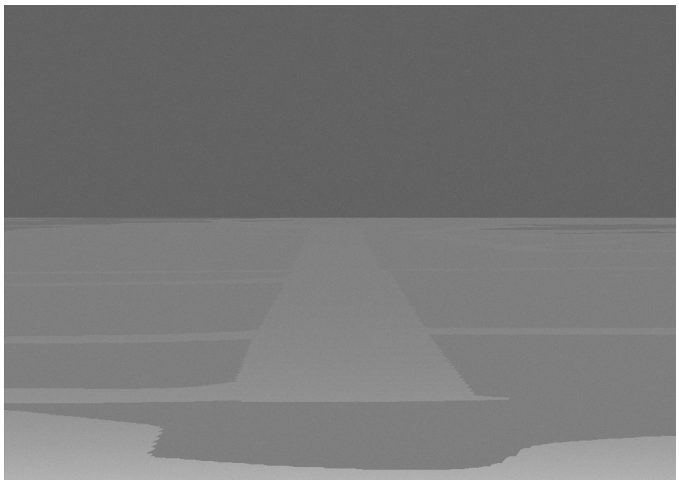

Figure 8.2: Simulated LWIR image of landing approach.

The effect of the lower transmittance for longer slant paths can be seen in the rear part of the runway. The contrast between the runway and the surrounding grass is quite low. However, in the beginning of the runway, the contrast is much better due to higher transmittance.

Below is an image taken with a real LWIR camera, see Figure 8.3. This image was taken during a landing approach in good weather conditions and the camera settings are not known. Thus, the constructed image and the real IR image can not be compared in detail, although it provides an idea of the performance of the simulator.

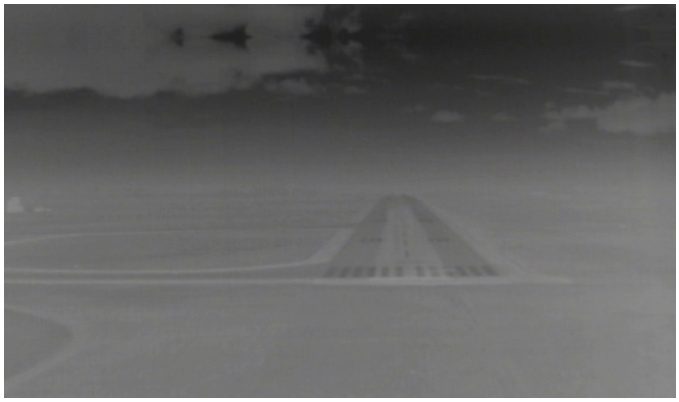

Figure 8.3: LWIR image of landing approach.

9 Discussion

9.1 Part I: Infrared transmittance in different weather conditions

From the transmission spectra, characteristics from the theory related to scattering and extinction can be seen. The relation between extinction and size parameter is especially interesting since the size distributions of the simulated aerosol models used in the simulations differ significantly. The attenuation is in most cases greater in the SWIR and MWIR parts of the spectrum, since most of the aerosols affecting the radiation have a size comparable to the wavelengths in those intervals. LWIR shows the greatest overall transmittance, although it is not as significant for aerosol models with broad size distributions such as advective fog.

Even though the visibility is equal for both fog types, the transmittance spectra looks anything but similar. The most obvious difference between the transmittance spectra for radiative and advective fog is the attenuation of the shorter wavelengths, i.e. less than 8 µm. The explanation is the significant difference between their size distributions. Radiative fog is characterized by a narrow distribution of smaller droplets, with radii in the range 1-10 µm. Advective fog on the other hand, has a much larger size range and therefore attenuates efficiently even in the LWIR portion of the spectrum.

From the surface temperature model it has been observed that a temperature difference of 1-3 degrees is common for different surface materials during winter time and corresponding latitude. In the case of radiative fog, the simulations show that a temperature difference of less than 1 degree can be seen at decision height in both CAT I, CAT II and CAT IIIa visibility conditions. For CAT IIIb, a 2 degree difference can be seen from 10 m. In all of these visibility conditions, the detection ranges in LWIR are superior to those in the visible wavelengths. Based on these simulations an IR camera operating in LWIR would be a meaningful aid. The results for advective fog on the other hand suggests that the defined sensors are unsatisfactory for all the investigated visibility conditions. As mentioned before, this is due to the relatively large size distribution responsible for the extensive scattering, even in LWIR.

For the different rain models, the simulation indicates no obvious improvement in IR compared to the visible spectrum for drizzle and heavy rain, but for light and moderate rain with the default MODTRAN cloud model. It is however difficult to accurately compare the detection ranges in visible and IR since the visibility is not defined in the MODTRAN rain models, although the attenuation is more or less equal throughout the investigated wavelengths. It's nevertheless clear that the transmittance is strongly dependent of the cloud modeling, particularly the cloud altitude. If the sensor's line of sight intersects the bottom of the cloud the transmittance is decreased due to cloud attenuation.

To be more realistic, the runway is probably not the first thing the pilot will see in adverse weather like thick fog or heavy rain. More likely is the visual contact with either the approaching lights or the touchdown zone lights prior to the actual runway. This is however beyond the scope of this study to investigate the actual visibility range with regard to what the pilot is actually able to see

in case of landing in poor visibility.

Based on the size distributions of different aerosols and fogs, together with the concept of size parameter and extinction, there is certainly an advantage in utilizing IR in some weather scenarios compared to light visible to the human eye. As has been discussed already, the highest level of extinction occurs when the particle radius is comparable to the wavelength of the incident light, and therefore other techniques would be more advantageous in cases with size distributions which scatters strongly in the IR range of the spectrum. PMMW and imaging radar are examples of techniques with longer wavelengths of radiation, in the millimeter range, and thus do not scatter as much in fog. Although, rain contains larger droplets which are likely to scatter millimeter wave radiation as well. For situations where fog and rain are not the limiting factors, but darkness, SWIR cameras could provide high resolution images of the runway and possible obstacles.

9.1.1 Future studies

In this study, only the MODTRAN predefined aerosol, fog and rain models were investigated, still, an useful option would be the user defined aerosol models, although a lot of data, including aerosol concentrations, size distributions and refractive indices etc. are required in order to define it in a realistic way. It would also be of great interest to further investigate the performance of IR cameras in case of snowfall, and to compare the IR detection range to the visibility.

9.2 Part II: Simulator for infrared imaging

9.2.1 Ground surface classification

As mentioned in Section 6.2, several approaches were evaluated in order to classify ground surfaces in satellite images. However, for the purpose of this study it was decided upon to proceed with a simple approach due to limited factors. The surfaces were binary classified as areas with surfaces for which emissivity data had been obtained. Since the most important contrast was considered to be between the runway and surrounding grass, the OpenStreetMap approach was considered to be sufficient. The surfaces were classified with high geographical resolution.

The classification was limited by several factors, first being the availability of emissivity data. Since only values for a few specific surface types were obtained, there was no point in doing a finer classification in that aspect. If more specific emissivity data had been obtained, more surface types could have been considered. For example, different fields of grassland might have different emissivity depending on the use of the land and the colour of it.

The ground surfaces were classified as polygon areas, which means that surfaces where several surface types might have been present were binary classified as the one most appropriate surface type. For example, a surface classified as grass might have been a mixture of soil and grass. Since the exact emissivity was not known for these types for surfaces, the classification was limited.

A finer classification would have been possible by using a machine learning approach together with the OpenStreetMap classification. The classification could have been finer and for example considered the boundary between different surfaces. It is not always realistic that the boundary between two surfaces is a sharp line, as assumed with the classification from OpenStreetMap.

By using a machine learning approach, large scale analysis of satellite images had been made possible to a larger extent. A trained algorithm might have been able to differentiate between different forest types, certain soil and vegetation types.

9.2.2 Performance of surface temperature model

From the validation of the surface temperature model, it can be observed that the model performance is varied in the different weather categories. However, the overall RMSE-values and MAE-values are rather low. In similar studies with surface temperature modelling, the performance of the models have been within an error margin of 4 °C.

There are several sources of error to consider regarding the surface temperature model, first being the emissivity constants used. It was difficult to obtain exact tabulated emissivity constants. In many cases, the emissivities were presented in intervals with a corresponding uncertainty value. The emissivity is also dependent on viewer angle, wavelength and the temperature of the surface or object. The emissivity has been considered constant and thus the model is simplified.

The weather parameters obtained from SMHI might not have matched the condition at the measurement site. The weather parameters used were obtained from Arlanda weather station, whereas the measurements were made outside Saab, in Järfälla. The local weather conditions can vary with regards to wind speed and incident solar radiation due to cloud cover, among other weather parameters.

Assumptions regarding the thermal conductivity have also been made. Moisture in the ground can change the conductive heat properties of a material. The soil below the surface has been classified as either dry or moist depending on the weather conditions and the value of the thermal conductivity, κ, has been altered correspondingly.

The surface temperature model considers the thermal conductivity from a layer temperature, T_{layer}, 10 cm below the surface according to the model referred to in Section 6.3. This temperature is, among other parameters, based on the average temperature the two previous days. This is the only time aspect taken into account by the surface temperature model. The model has no short time aspect, which could be an important factor to consider when clouds suddenly sweep in, for instance when the sun has been heating the surface for a period of time.

Another factor to consider is the accuracy of the thermal camera, $\pm$ 2°C. It's difficult to know if the reference measurements are comparable to the temperatures provided by the model. The camera also assumes a constant emissivity of 0.95 for all surfaces, which is relatively close to the emissivity constants of the surfaces considered.

It was difficult to make a correct temperature reading from the camera display, since the different surfaces had local variations in the temperature. Although in attempt to reduce random errors, several measurements were made for every surface type during each measurement session.

The overall performance of the surface temperature model is considered acceptable for the studied conditions based on the RMSE and MAE values presented in Section 8.2. However, to make the model more robust, the thermal conductivity and time aspect should be further investigated. Since time was limited for this study, the temperature data collected were confined. More data would be necessary to further validate the model.

9.2.3 Overall simulation performance

As seen in the simulated image landing approach image in Section 8.3, it is possible to distinguish the runway from the surrounding surfaces. Even though the contrast is rather low, it is possible to see the outline of the actual runway.

This simulation model is very simplified in the sense of surface classification and thus the contrasts between two surfaces may appear more distinct than reality. For the same reason there are not different shades in a specific surface class in the simulated IR image. By developing a more detailed surface classification, the image would contain more intensity variations and thus appear more realistic, although the contrast between the runway and the surroundings might be somewhat reduced. As previously discussed, the surface temperature model has several sources of errors, and therefore the contrast may be affected.

The quality of the image is strongly dependent on the camera specifications and can thus vary quite a lot. In this particular simulation a LWIR camera with NETD = 20 mK was chosen, although, as previously mentioned the stated NETD is determined for a specific temperature and the approximation of a constant NETD might affect the resulting image. The SiTF was chosen based on temperature differences that could be observed in the scene. The gain is an important factor as well, with the ability to increase the contrast, up until the limitation of the NETD.

A 3D structure of the ground surface is another factor that would make the image more realistic. Although it implies scattering from tall objects which must be considered.

A comparison of the constructed IR image and a real IR image of the same view was presented in Section 8.3, which provides an idea of the performance of the simulator. The weather conditions were however dissimilar and the camera characteristics unknown, thus a detailed comparison was therefore not possible. In order to fully validate the outcome of the simulation in terms of contrast, a comparison between a real infrared camera image from an aircraft approach in adverse weather with well known camera specifications and settings, and the simulation constructed image for similar weather parameters would need to be made. However, based on the case that was simulated, there should be enough contrast to see the runway by theoretically considering the target temperature difference, the transmittance through the atmosphere and the NETD of the camera.

9.2.4 Data available online

Part of the objective of this study was to use data obtained online and therefore the larger part of the data used has been collected from online sources. Open source data is not always well structured, and sometimes many different sources must be combined in order to cover everything of interest. In some cases, the data necessary was not found completely. With that in mind, some compromises had to be made, for example the ground surface classification. A 2D classification can be retrieved from, or manually done, by OpenStreetMap. However, no open source option was found for a 3D view. Further, the emissivity data was a limiting factor for the surface classification since a more comprehensive classification would not have been utilized fully without more detailed emissivity data.

Weather data is relatively easy to access online. SMHI offers well structured data of many different weather parameters such as air temperature, wind speed and direction as well as solar irradiation. The data is frequently sampled and has been collected for a long period of time. Other sources requires efforts in manipulating the data in order to convert it to the right format.

Software to simulate the radiative transfer available online, were either found to be insufficient for the purpose, in terms of resolution, or difficult to use. Therefore the simulation software MODTRAN was purchased.

9.2.5 Future studies

Due to limited time and resources, some simplifications had to be made. Further improvements could be done to the ground surface classification as well as the surface temperature model. If more detailed emissivity data could be retrieved or measured, the surface classification could also be improved. For example, machine learning or artificial intelligence could be very beneficial. The surface temperature model could be further improved with better conduction modeling and more sensitive time dependence etc. A proper validation, or comparison of the final simulation image to an actual IR image from an aircraft approach in similar weather conditions is also highly desirable.

10 Conclusions

The transmittance of IR differ substantially between different weather conditions. This is strongly correlated to the size distribution of the particles suspended in the atmosphere. This investigation has shown that the detection range in LWIR is almost 4 times the visibility in radiative fog, and therefore a LWIR cameras can be a beneficial component in EFVS in such weather scenarios. For advective fog and rain, the extinction is however more homogeneous throughout the visible and IR wavelengths and thus, IR cameras exhibit no obvious advantage. In such cases, other techniques, like imaging radar which utilize radiation of longer wavelengths, are likely to have better weather penetrating abilities, although that is at the expense of the resolution.

It is possible to create an imaging simulation environment for the generation of IR images. However, in this investigation many simplifications were made and in order to create a more accurate image, further development of the different modules would be necessary. It is also desirable to make the simulation in real time.

The overall conclusion from this thesis project is that using complementary camera sensors outside the visible spectrum can help pilots during landing approaches in adverse weather conditions, like fog and precipitation.

References

[1] Zhao-Liang Li et al. Satellite-derived land surface temperature: Current status and perspectives. *Remote Sensing of Environment*, 2013.

[2] Emma Dodd, Karen Veal, and Darren Ghent. Satellite LST User Handbook. http://www.globtemperature.info/index.php/public-documentation/deliverables-1/215-lst-handbook/file, 2016. [Online; accessed 2019-03-12].

[3] Maxime E. Bonjeana, Fabian D. Lapierre, Jens Schiefelec, and Jacques G. Verlya. Flight Simulator with IR and MMW Radar Image Generation Capabilities. *Proceedings of SPIE - The International Society for Optical Engineering*, 2006.

[4] Ni Li, Wenqing Huai, Shaodan Wang, and Lei Ren. A real-time infrared imaging simulation method with physical effects modeling of infrared sensors. *Infrared Physics Technology*, 78:45–77, 2016.

[5] John Lester Miller, Richard Kerr, James L. Gates, and Terry Dickerson. Runway-based infrared sensor for enhanced vision of approaching aircraft. *Enhanced and Synthetic Vision 2000*, 2000.

[6] Williamson Corporation. Infrared Energy, Emissivity, Reflection & Transmission. https://www.deltat.com/pdf/Infrared\%20Energy,\%20Emissivity,\%20Reflection\%20\%26\%20Transmission.pdf. [Online; accessed 2019-02-06].

[7] InfraTec GmbH Infrarotsensorik und Messtechnik. Infrared Radiation. https://www.infratec.eu/sensor-division/service-support/glossary/infrared-radiation/, 2019. [Online; accessed 2019-05-16].

[8] Dr Alexander and A. Kokhanovsky. *Aerosol Optics: Light Absorption and Scattering by Particles in the Atmosphere*. Springer Berlin Heidelberg, ISBN:1-281-23958-5, 2008.

[9] Kuo-Nan Liou. *An introduction to atmospheric radiation*. Amsterdam ; Boston : Academic Press, ISBN: 0-08-049167-7, 2002.

[10] David W. Hahn. Light Scattering Theory. *Department of Mechanical and Aerospace Engineering, University of Florida*, 2009.

[11] Lingbing Bu, Kunling Shan, Xingyou Huang, and Li Guan. Mie theory and its application in probe of cloud droplet. *SPIE Digital Library - Proceedings*, 2009.

[12] Michael Kotlarchyk. *Encyclopedia of Spectroscopy and Spectrometry*. Elsevier Ltd, ISBN: 978-0-12-374413-5, 2010.

[13] M. Mishchenko, L. Travis, and A. Lacis. *Encyclopedia of Atmospheric Sciences*. Elsevier Ltd, ISBN: 978-0-12-382225-3, 2015.

[14] M. Mishchenko, L. Travis, and A. Lacis. Multiple Scattering of Light by Particles. *Cambridge University Press*, 2006.

[15] Kurt Beier and Hans Gemperlein. Simulation of infrared detection range at fog conditions for Enhanced Vision Systems in civil aviation. *Aerospace Science and Technology*, 2004.

[16] Climate Science Investigations. The Greenhouse Effect. http://www.ces.fau.edu/nasa/module-2/how-greenhouse-effect-works.php. [Online; accessed 2019-02-06].

[17] Frederick G. Smith. *The Infrared Electro-Optical Systems Handbook, Volume 2: Atmospheric Propagation of Radiation*. Ann Arbor, Mich. ; Bellingham, Wash. : Infrared Information Analysis Center: SPIE Optical Engineering Press, 1993.

[18] NC State University Climate Office. Composition of the Atmosphere. https://climate.ncsu.edu/edu/Composition. [Online; accessed 2019-02-06].

[19] GIS Geography. Why the atmospheric window matters in earth science. https://gisgeography.com/atmospheric-window/, 2018. [Online; accessed 2019-02-06].

[20] FLIR Commercial Vision Systems B.V. Seeing through fog and rain with a thermal imaging camera, Metrological effects of Fog Rain upon IR Camera Performance. [Online; accessed 2019-03-29].

[21] Eric P. Shettle and Robert W. Fenn. Models for the aerosols of the lower atmosphere and the effects of humidity variations on their optical properties. *Enverionmental Research Papers, NO 676*, 1979.

[22] Experimental Aircraft Info. Advection fog formation. https://www.experimentalaircraft.info/wx/weather-fog-1.php, 2019. [Online; accessed 2019-03-29].

[23] Naturskyddsföreningen. Faktablad: Albedo. https://www.naturskyddsforeningen.se/skola/energifallet/faktablad-albedo, 2017. [Online; accessed 2019-02-06].

[24] George J. Zissis. *The Infrared Electro-Optical Systems Handbook, Volume 1: Sources of Radiation*. Ann Arbor, Mich. ; Bellingham, Wash. : Infrared Information Analysis Center: SPIE Optical Engineering Press, 1993.

[25] Federal Aviation Administration. Ground-Based Navigation - Instrument Landing System (ILS). https://www.faa.gov/about/office_org/headquarters_offices/ato/service_units/techops/navservices/gbng/ils/, 2016. [Online; accessed 2019-06-03].

[26] Decision Altitude/Height (DA/DH). https://www.skybrary.aero/index.php/Decision_Altitude/Height_(DA/DH), 2017. [Online; accessed 2019-06-03].

[27] Andrew Wood. Alternatives to ILS gaining momentum. https://www.ainonline.com/aviation-news/2007-12-27/alternatives-ils-gaining-momentum, 2007. [Online; accessed 2019-06-03].

[28] Airbus. Getting to grips with CAT II / CAT III operations. https://www.skybrary.aero/bookshelf/books/1480.pdf.

[29] Maxime E. Bonjeana, Jens Schiefelec, and Jacques G. Verlya. Multisensor Flight Simulation with Emphasis on Synthesis of IR Imagery. 2005.

[30] Randall E. Bailey. The Use of Enhanced Vision Systems for See-and-Avoid During Surface Operations. 2016.

[31] Federal Aviation Administration. Revisions to Operational Requirements for the Use of Enhanced Flight Vision Systems (EFVS) and to Pilot Compartment View Requirements for Vision Systems. Federal Register/Vol 81, No. 239, December, 2016.

[32] Sensors Unlimited. Why SWIR? http://www.sensorsinc.com/technology/why-swir. [Online; accessed 2019-05-06].

[33] John Wallace. SWIR cameras cut through haze for surveillance and security. *Laser Focus World*, March 2019.

[34] Alfredo Petrosino. *Progress in Image Analysis and Processing, ICIAP 2013 : Naples, Italy, September 9-13, 2013, Proceedings, Part II*. Springer Berlin Heidelberg, 2013.

[35] N. Gopalsami et al. Evaluation of passive millimeter wave system performance in adverse weather conditions. *Proceedings of SPIE*, 2012.

[36] Tony Freeman. What is Imaging Radar? https://airsar.jpl.nasa.gov/documents/genairsar/radar.html. [Online; accessed 2019-05-06].

[37] Velodyne Lidar. How LiDAR Technology Enables Autonomous Cars to Operate Safely. https://velodynelidar.com/newsroom/how-lidar-technology-enables-autonomous-cars-to-operate-safely/, 2018. [Online; accessed 2019-05-06].

[38] Matti Kutila et al. Automotive LiDAR performance verification in fog and rain. *IEEE*, 2018.

[39] Elprocus. Infrared IR Sensor Circuit Diagram and Working Principle. https://www.elprocus.com/infrared-ir-sensor-circuit-and-working/, 2018. [Online; accessed 2019-05-10].

[40] MoviTHERM. Thermal Infrared Imaging explained. http://movitherm.com/knowledgebase/thermal-infrared-imaging-explained/. [Online; accessed 2019-05-10].

[41] FLIR Systems AB. *The Ultimate Infrared Handbook for RD Professionals*. FLIR AB, Reading, Massachusetts, 2018.

[42] Hamamatsu. Characteristics and use of infrared detectors. https://www.hamamatsu.com/resources/pdf/ssd/infrared_kird9001e.pdf, 2011. [Online; accessed 2019-05-06].

[43] Alexander Chilton. The Working Principle and Key Applications of Infrared Sensors. https://www.azosensors.com/article.aspx?ArticleID=339, 2014. [Online; accessed 2019-02-07].

[44] Thomas Williams. *The Optical Transfer Function of Imaging Systems*. Institute of Physics Publishing, 1999.

[45] MoviTHERM. What is NETD in a Thermal Camera?. http://movitherm.com/knowledgebase/netd-thermal-camera/. [Online; accessed 2019-06-01].

[46] Openstreetmap Foundation. About the OpenStreetMap Foundation. https://wiki.osmfoundation.org/wiki/Main_Page.

[47] J. B. Campbell and R. H. Wynne. *Introduction to Remote Sensing*. Guilford Press , New York, USA, 1997.

[48] ThermoView. Emissivity Tables. http://www.thermoview.ru/pdf/emis3.pdf. [Online; accessed 2019-02-22].

[49] ThermoWorks. Emissivity Table. https://www.thermoworks.com/emissivity_table. [Online; accessed 2019-02-22].

[50] E. Rubio, V. Caselles, and C. Badenas. Emissivity measurements of several soils and vegetation types in the 8–14, μm Wave band: Analysis of two field methods. *Remote Sensing of Environment*, 1997.

[51] Assessing the thermal properties of dry and saturated soils using the TLS - 100 Portable Thermal Resistivity Meter. https://thermtest.com/applications/soil-thermal-conductivity-tls.

[52] Thermal Conductivity of common Materials and Gases. https://www.engineeringtoolbox.com/thermal-conductivity-d_429.html.

[53] SMHI. Hur mäts globalstrålning. https://www.smhi.se/kunskapsbanken/meteorologi/hur-mats-globalstralning-1.77050.

[54] SMHI. Hur mäts vind. https://www.smhi.se/kunskapsbanken/meteorologi/hur-mats-vind-1.5924.

[55] SMHI. Hur mäts lufttemperatur. https://www.smhi.se/kunskapsbanken/meteorologi/hur-mats-lufttemperatur-1.3839.

[56] A. Berk et al. MODTRAN6: a major upgrade of the MODTRAN radiative transfer code. *Proc. SPIE*, 2014.

[57] A. Berk et al. MODTRAN®6.0 User's Manual, 2018.

[58] B.A Silverman and E.D Sprague. Airborne measurement of in-cloud visibility. *American Meteorological Society*, 1970.

[59] Finn Plauborg. Simple model for 10 cm soil temperature in different soils with short grass. *European Journal of Argonomy*, 2002.

[60] Fluke Corporation. Fluke Ti10 Infrared Camera. https://www.fluke.com/en-us/product/thermal-cameras/ti10.

[61] A. Berk et al. Algorithm Theoretic Basis Document (ATBD) for next generation MODTRAN®, 2016.

Appendix

Radiative transfer in MODTRAN

Radiative transfer is the physical process when energy is transferred in the form of electromagnetic radiation. The propagation of infrared radiation through the atmosphere is affected by absorption, scattering and emission processes. The radiative transfer equation describes these interactions mathematically [9].

The intensity of the propagating radiation, I_λ, is reduced by absorption and scattering along the path.

$$dI_\lambda = -k_\lambda \rho I_\lambda ds \tag{1}$$

k_λ is the mass extinction cross section and ρ the density of the medium. The intensity is further increased by emission and multiple scattering into the beam.

$$dI_\lambda = j_\lambda \rho ds \tag{2}$$

With j_λ defined as the source function coefficient, with the same physical meaning as the mass extinction cross section. By combining Equation 1 and 2 the following expression is obtained

$$dI_\lambda = -k_\lambda \rho I_\lambda ds + j_\lambda \rho ds. \tag{3}$$

By defining the source function J_λ as

$$J_\lambda \equiv j_\lambda / k_\lambda \tag{4}$$

the radiative transfer equation can thus be expressed as follows

$$\frac{dI_\lambda}{k_\lambda \rho ds} = -I_\lambda + J_\lambda. \tag{5}$$

Moreover,

$$\tau = \int k_\lambda \rho ds, \tag{6}$$

τ is the optical depth. This generates the final expression for the radiative transfer equation

$$\frac{dI_\lambda}{d\tau} = -I_\lambda + J_\lambda. \tag{7}$$

The following theory is based on the MODTRAN documentation [61] and describes the physics of radiative transfer used to model atmospheric propagation in MODTRAN.

At every modeled spectral point, molecular and particulate extinction coefficients must be generated. These coefficients depend on pressure and temperature pairs in the atmosphere. The contributions from other molecular transitions far away from the considered spectral point must be taken into account. The radiative transfer equation can be solved for individual spectral points when the extinction data has been defined. Due to the fine structure of molecular absorption, the spectral grid must be very finely spaced. Usually a step size between 0.01 and 0.00001 cm^{-1} is required, depending on the desired accuracy.

The solution of the radiation transfer equation in MODTRAN is defined by the line-of-sight monochromatic radiant intensity $I_0(\Omega_0;\nu)$. ν is the spectral frequency along the path from the sensor (path length l=0) and in the viewing direction of the sensor $\Omega_0 \equiv (\mu_0, \phi_0)$:

$$I_0(\Omega_0;\nu) = exp[-\tau_l(\nu)]I_l(\Omega_l;\nu) + \int_0^{\tau_l(\nu)} exp[-\tau_{l'}(\nu)]J_{l'}(\Omega_{l'};\nu)d\tau_{l'}(\nu) \tag{8}$$

The spectral radiance at the sensor is the sum of two terms, according to Equation 8. The first term corresponds to the boundary term, which is the product of the spectral transmittance, $exp[-\tau_l(\nu)]$, and the spectral radiant intensity, $I_l(\Omega_l;\nu)$. The spectral transmittance is the result of extinction in the path and the spectral radiant intensity is the intensity directed toward the sensor at path length, l, along the line-of-sight. The second term corresponds to the path radiance, which is the integral over the source radiation directed toward the sensor, $J_{l'}(\Omega_{l'};\nu)$, and the foreground transmittance, $exp[-\tau_{l'}(\nu)]$.

As seen in Equation 8, the path spectral transmittances decrease exponentially with the dimensionless extinction optical depth, $\tau_l(\nu)$. These terms are path integrals over extinction coefficients, $b_{l'}(\nu)$:

$$\tau_l(\nu) \equiv \int_0^l b_{l'}(\nu)dl' \tag{9}$$

The extinction coefficients consider both absorption $b_l^{abs}(\nu)$ and scattering $b_l^{sct}(\nu)$ from different molecules and particles in the atmosphere. These are computed as sums from the species contributions, $b_{l,i}(\nu)$:

$$b_l(\nu) \equiv b_l^{abs}(\nu) + b_l^{sct}(\nu) \equiv \sum_{i\ species} [b_{l,i}^{abs}(\nu) + b_{l,i}^{sct}(\nu)] \equiv \sum_{i\ species} [\kappa_{l,i}^{abs}(\nu) + \kappa_{l,i}^{sct}(\nu)]\rho_i(l) \tag{10}$$

The absorption and scattering coefficients for different species are computed as the cross-section $\kappa_{l,i}(\nu)$ (area dimension) times the density $\rho_i(l)$ (number per unit volume). The optical depth of absorption and scattering are defined as:

$$\tau_l^{abs}(\nu) \equiv \int_0^l b_{l'}^{abs}(\nu) dl' \quad and \quad \tau_l^{sct}(\nu) \equiv \int_0^l b_{l'}^{sct}(\nu) dl' \tag{11}$$

By differentiating Equation 9 and Equation 11 and solving for the differential path length, dl, the following relationship can be generated:

$$dl = \frac{d\tau_l(\nu)}{b_l(\nu)} = \frac{d\tau_l^{abs}(\nu)}{b_l^{abs}(\nu)} = \frac{d\tau_l^{sct}(\nu)}{b_l^{sct}(\nu)} \tag{12}$$

The atmospheric source term in Equation 8, $J_l(\Omega_l;\nu)$, in MODTRAN has three different components:

$$J_l(\Omega_l;\nu) = J_l^{em}(\Omega_l;\nu) + J_l^{ss}(\Omega_l;\nu) + J_l^{ms}(\Omega_l;\nu) \tag{13}$$

- Local thermal emission:
  $J_l^{em}(\Omega_l;\nu) = \frac{b_l^{abs}(\nu)}{b_l(\nu)} B(T_l;\nu)$
- Directly transmitted single scattered solar (or lunar) irradiance:
  $J_l^{ss}(\Omega_l;\nu) = \frac{b_l^{sct}(\nu)}{b_l(\nu)}\, p_l(\Omega_l, \Omega_l^{sun};\nu)\, exp[-\tau_l^{sun}(\nu)]\, F^{sun}(\nu)$
- Diffuse radiation scattered into the line-of-sight:
  $J_l^{ms}(\Omega_l;\nu) = \frac{b_l^{sct}(\nu)}{b_l(\nu)} \int_{4\pi} p_l(\Omega_l, \Omega_l';\nu)\, I_\nu(\Omega_l',\nu)\, d\Omega_l'$

The thermal emission is a product of the Plank blackbody function $B(T_l;\nu)$ with temperature T_l and the ratio of absorption to extinction coefficients which corresponds to the local emissitivty.

The single scatter solar radiation contributes to the path scattered radiance. It is the product of top-of-atmosphere solar irradiance $F^{sun}(\nu)$, the point of scattering to sun transmittance $exp[-\tau_l^{sun}(\nu)]$, the effective scattering phase function $p_l(\Omega_l, \Omega_l^{sum};\nu)$, and the ratio of scattering to extinction coefficients, which corresponds to the single scattering albedo.

The multiple scattered radiation also contributes to the path scattered radiance. It is an integral over all directions, 4π steradians, of diffuse radiation that is scattered into the line-of-sight. The radiation transport equation is very complicated due to the effect multiple scattering have on the total path radiance. This is due to the fact that source and radiant intensity terms are coupled. MODTRAN has three different algorithms to solve these coupled equations, the most commonly used being the high fidelity DISORT, discrete ordinate algorithm.

The effective phase function, $p_l(\Omega_l, \Omega_l';\nu)$, that is present in both radiance source terms in Equation 13 is the weighted average of the scattering coefficient based on the individual species i scattering phase functions $p_{l,i}(\Omega_l, \Omega_l';\nu)$:

$$p_l(\Omega_l, \Omega_l';\nu) \equiv \frac{\sum_{i\ species}\ b_{l,i}^{sct}\ p_{l,i}(\Omega_s, \Omega';\nu)}{b_l^{sct}(\nu)} \tag{14}$$

Equation 13 can be substituted into the spectral radiant intensity of Equation 8.

$$
\begin{aligned}
I_0(\Omega_0;\nu) &= exp[-\tau_l(\nu)] I_l(\Omega_l;\nu) \\
+ \int_0^{\tau_l(\nu)} exp[-\tau_{l'}(\nu)] \Bigg[& \frac{b_l^{abs}(\nu)}{b_l(\nu)} B(T_l;\nu) + \frac{b_l^{sct}(\nu)}{b_l(\nu)} \, p_l(\Omega_l, \Omega_l^{sun};\nu) \, exp[-\tau_l^{sun}(\nu)] \, F^{sun}(\nu) \\
& + \frac{b_l^{sct}(\nu)}{b_l(\nu)} \int_{4\pi} p_l(\Omega_l, \Omega_l';\nu) \, I_\nu(\Omega_l',\nu) \, d\Omega_l' \Bigg] d\tau_{l'}(\nu)
\end{aligned}
\tag{15}
$$

The integrals can be written as integrals over absorption optical depth, $\tau_l^{abs}(\nu)$, and scattering optical depth, $\tau_l^{sct}(\nu)$. Here, the relationships of Equation 12 have been used.

$$
\begin{aligned}
I_0(\Omega_0;\nu) = exp[-\tau_l(\nu)] I_l(\Omega_l;\nu) & + \int_0^{\tau_l^{abs}(\nu)} exp[-\tau_{l'}(\nu)] \, B(T_{l'},\nu) \, d\tau_{l'}^{abs}(\nu) \\
+ \int_0^{\tau_l^{sct}(\nu)} exp[-\tau_{l'}(\nu)] \Bigg[& p_{l'}(\Omega_{l'}, \Omega_{l'}^{sun};\nu) \, exp[-\tau_{l'}^{sun}(l')] \, F^{sun}(\nu) + \\
& \int_{4\pi} I_{l'}(\Omega_{l'}';\nu) \, p_{l'}(\Omega_{l'}, \Omega_{l'}';\nu) \, d\Omega_{l'}' \Bigg] \, d\tau_{l'}^{sct}(\nu)
\end{aligned}
\tag{16}
$$

The most important atmospheric attenuation quantity in band model theory is the transmittance and not the optical depth. The radiative transfer function can therefore be expressed in the terms of transmittance instead, $t_l(\nu) = exp[-\tau_l(\nu)]$. The relationship between optical depth and transmittance can be defined by the following expressions:

$$
\begin{aligned}
t_l^{abs}(\nu) = exp[-\tau_l^{abs}(\nu)] \quad &\longrightarrow \quad dt_l^{abs} = -d\tau_l^{abs}(\nu) \, exp[-\tau_l^{abs}(\nu)] = -t_l^{abs}(\nu) \, d\tau_l^{abs}(\nu) \\
t_l^{sct}(\nu) = exp[-\tau_l^{sct}(\nu)] \quad &\longrightarrow \quad dt_l^{sct} = -d\tau_l^{sct}(\nu) \, exp[-\tau_l^{sct}(\nu)] = -t_l^{sct}(\nu) \, d\tau_l^{abs}(\nu) \\
&\Longrightarrow \quad -t_l^{sct}(\nu) dt_l^{abs}(\nu) = exp[-\tau_l(\nu)] \, d\tau_l^{abs}(\nu) \\
&\Longrightarrow \quad -t_l^{abs}(\nu) dt_l^{sct}(\nu) = exp[-\tau_l(\nu)] \, d\tau_l^{sct}(\nu)
\end{aligned}
\tag{17}
$$

The transmittance dependent radiative transfer equation can be expressed by inserting expressions from Equation 17 into Equation 16:

$$
\begin{aligned}
I_0(\Omega_0;\nu) &= t_l(\nu) \, I_l(\Omega_l;\nu) + \int_{t_l^{abs}(\nu)}^{1} t_{l'}^{sct}(\nu) \, B(T_{l'},\nu) \, dt_{l'}^{abs}(\nu) \\
+ \int_{t_l^{sct}(\nu)}^{1} t_{l'}^{abs}(\nu) & \Bigg[p_{l'}(\Omega_{l'}, \Omega_{l'}^{sun};\nu) \, t_{l'}^{sun}(\nu) \, F^{sun}(\nu) + \int_{4\pi} I_{l'}(\Omega_{l'}';\nu) \, p_{l'}(\Omega_{l'}, \Omega_{l'}';\nu) \Bigg] \, dt_{l'}^{sct}(\nu)
\end{aligned}
\tag{18}
$$

The radiant intensity at the end of the line-of-sight path, $I_l(\Omega_l;\nu)$, is typically zero in MODTRAN if the path doesn't terminate at some surface. Both emissive and reflective factors are included in the surface radiance.

$$
\begin{aligned}
I_s(\Omega_s;\nu) = \epsilon_s(\Omega_s;\nu) \, B(T_g,\Omega) + \mu_s^{sun} F_s(\Omega_s, \Omega_s^{sun};\nu) \, t_s^{sun}(\nu) \, F^{sun}(\nu) \\
+ \int_{2\pi} I_s(\Omega_s';\nu) \, f_s(\Omega_s, \Omega_s';\nu) \, \mu_s' d\Omega_s'
\end{aligned}
\tag{19}
$$

In this equation, $\epsilon_s(\Omega_s;\nu)\, B(T_g,\Omega)$ corresponds to the surface emission, $\mu_s^{sun} F_s(\Omega_s,\Omega_s^{sun};\nu)\, t_s^{sun}(\nu)\, F^{sun}(\nu)$ corresponds to the reflected part of the directly transmitted solar irradiance and $\int_{2\pi} I_s(\Omega_s';\nu)\, f_s(\Omega_s,\Omega_s';\nu)\, \mu_s' d\Omega_s'$ corresponds to the surface reflected downward flux. The variables are defined at a distance l=s from the sensor along the line-of-sight, and depend on the surface on the ground.

The Earth viewing radiance, observed by a sensor, is given by substituting the surface radiance term, Equation 19, into the radiative transfer equation, Equation 18.

$$I_0(\Omega;\nu) = t_l(\nu)\, I_l(\Omega;\nu) + \int_{t_l^{abs}(\nu)}^{1} t_{l'}^{sct}(\nu)\, B(T_{l'},\nu)\, dt_{l'}^{abs}(\nu)$$
$$+ \int_{t_l^{sct}(\nu)}^{1} t_{l'}^{abs}(\nu) \left[\begin{array}{l} \mathrm{t}_{l'}^{sun}(\nu)\, F^{sun}(\nu)\, p_{l'}(\Omega,\Omega_{sun};\nu) \\ \\ +\ \int_{4\pi} I_{l'}(\Omega';\nu)\, p_{l'}(\Omega,\Omega';\nu)\, d\Omega' \end{array} \right] dt_{l'}^{sct}(\nu)$$

$$\mathrm{I}_l(\Omega;\nu) = \begin{cases} 0 \quad \text{if l is at the top of the atmosphere} \\ \\ \epsilon_s(\Omega;\nu)\, B(T_g,\nu) + \int_{2\pi} \left[t_s^{sun}(\nu) \frac{F^{sun}(\nu)}{\pi}\, \delta(\Omega-\Omega^{sun}) + I_s(\Omega',\nu) \right] f_s(\Omega,';\nu) \mu' d\Omega' & if\ l = s \end{cases} \tag{20}$$

In MODTRAN, the statistic band model integrates the radiative transfer over small spaced spectral bins. The radiant intensity observed by a sensor is therefore defined by:

$$\left\langle I_0(\Omega) \right\rangle \equiv \frac{1}{\Delta\nu} \int_{\Delta\nu} I_0(\Omega,\nu) d\nu \tag{21}$$

The purpose of the band model is to accurately model the total absorption in each spectral bin due to all molecular transitions that take place. The MODTRAN bins have a width, $\Delta\nu$, of 0.1, 1.0, 5.0 or 15 cm^{-1}. In every bin, particle scattering/absorption and Rayleigh scattering are considered.

TRITA 2019:109